The Microbe 3 (2024) 100059

Contents lists available at ScienceDirect

The Microbe

journal homepage: www.sciencedirect.com/journal/the-microbe

Investigation of some plant stilbenoids and their fragments for the identification of inhibitors of SARS-CoV-2 viral spike/ACE2 protein binding

Cyril T. Namba-Nzanguim [a,b], Conrad V. Simoben [a], Boris D. Bekono [c], Ian Tietjen [d], Joel Cassel [d], Joseph M. Salvino [d], Luis J. Montaner [d], Rohan A. Davis [e], Fidele Ntie-Kang [a,b,f,*]

[a] Center for Drug Discovery, Faculty of Science, University of Buea, P. O. Box 63, Buea, Cameroon
[b] Department of Chemistry, Faculty of Science, University of Buea, P. O. Box 63, Buea, Cameroon
[c] Department of Physics, Ecole Normale Superieure, University of Yaoundé 1, P. O. Box 47, Yaoundé, Cameroon
[d] The Wistar Institute, Philadelphia, PA, USA
[e] Griffith Institute for Drug Discovery, School of Environment and Science, Griffith University, Brisbane, QLD, Australia
[f] Institute of Pharmacy, Martin-Luther University Halle-Wittenberg, Kurt-Mothes-Str. 3, Halle (Saale) 06120, Germany

ARTICLE INFO

Keywords:
Docking
Molecular dynamics
Natural product
Stilbenoid fragment
Spike/ACE2

ABSTRACT

In silico binding studies were conducted on the known plant-derived polyphenolic tetrameric stilbenoids, (–)-hopeaphenol (**1**), vaticanol B (**2**) and vatalbinoside A (**3**) and their monomeric derivative resveratrol (**8**), identified from several plant species. The natural products (NPs) **1**–**3** had been previously evaluated against the SARS-CoV-2 protein targets responsible for viral transmission and infection. The two isomeric compounds (–)-hopeaphenol and vaticanol B had displayed a high affinity for blocking the binding of the SARS-CoV-2 viral spike with the human angiotensin-converting enzyme 2 (ACE2). Molecular docking and molecular dynamics simulations have been used to attempt to explain the affinity of the compounds to the spike/ACE2 complex. The hydrophobic properties of the respective target sites were computed and compared with the physicochemical properties of the NPs to explain the affinity of each compound toward the target site. Molecular docking and computed ADMET/DMPK profiles were also used to demonstrate the potential of the NPs and their fragments as possible lead compounds for antiviral discovery. These results support the experimental data obtained to date on **1**–**3** and clearly identify the stilbenoid structure class as one worthy of future studies during chemical biology and/or drug discovery antiviral efforts.

1. Introduction

In silico (computer-based) methods for drug discovery cover a broad array of structure-based and ligand-based approaches (Ferreira et al. 2015; Vázquez et al. 2020; Ntie-Kang et al., 2016). The former mostly exploits the available three-dimensional (3D) structures of target receptors, being focused on the analysis of drug-receptor interactions and providing clues for explaining observed biological activities of small molecules that might be developed into drugs (Meek and Weaver, 2022). Amongst the most cited methods for structure-based drug design methods is molecular docking (Chen, 2015; Morris and Lim-Wilby, 2008; Lohning et al. 2017), which attempts to predict the orientation of a small molecular entity within a receptor site. The advantage is that docking is often followed by scoring methods (or mathematical algorithms) that attempt to quantify the interactions between the atoms of the small molecule and those of the receptor site (Arcon et al. 2021; Esmaielbeiki & Nebel, 2014; Kontoyianni, 2017; Rogers et al. 2023; Bekono et al., 2018). Scoring methods are mathematical methods for quantifying protein-ligand interactions, hence are often used to discriminate between active and inactive compounds from large compound libraries. This process is known as virtual screening (Baig et al. 2016; Kontoyianni, 2017; Lionta et al. 2014), but can as well be useful in suggesting analogues of a bound small molecule that could interact favourably with the target receptor based on the observed drug-target interactions in 3D space (Baig et al. 2016; Urbina et al. 2022; Wermuth, 2006). The clear advantage of such an approach is the cost-effectiveness and timeliness when compared to wet lab experiments (Horvath, 2011; Kontoyianni, 2017; Macalino et al. 2015; Sciabola et al. 2022; Tripathi and Bandyopadhyay, 2022; Wermuth, 2006). With the increased speed with which high-quality 3D protein structures of drug

* Corresponding author at: Center for Drug Discovery, Faculty of Science, University of Buea, P. O. Box 63, Buea, Cameroon.
E-mail address: fidele.ntie-kang@ubuea.cm (F. Ntie-Kang).

https://doi.org/10.1016/j.microb.2024.100059
Received 15 January 2024; Received in revised form 28 February 2024; Accepted 21 March 2024
Available online 23 March 2024

targets are being obtained, often with co-crystallized small molecules, the explosion of new protein structures deposited in the RCSB protein data bank (PDB) (Berman et al. 2000; Burley et al. 2017; Burley et al. 2018) provides an open platform for *in silico* drug discovery.

With the advent of the COVID-19 pandemic caused by Severe Acute Respiratory Syndrome Coronavirus2 (SARS-CoV-2), the rapid availability of X-ray crystallography structures of SARS-CoV-2 protein drug targets resulted in a wealth of published *in silico* hits (Moumbock et al. 2023). Most of the published hits were based on molecular docking studies, often coupled with molecular dynamics (MD) used to study the stability of the structures of drug targets in the presence of small molecules or based on the receptor-small molecule interactions (Ghosh et al. 2021; Moumbock et al. 2023; Pipitò et al. 2022; Shadrack et al. 2021; Tanimoto et al. 2022; Vuai et al., 2022).

Among the most investigated drug targets of interest in SARS-CoV-2 are the main protease (M^{pro}) and the viral spike that binds with the human angiotensin-converting enzyme 2 (ACE2) involved in the transmission of the virus (Arya et al. 2021; Jackson et al. 2022). Since the discovery of the parental Wuhan variant of SARS-CoV-2, several mutations in the receptor binding domain (RBD) of the SARS-CoV-2 viral spike have arisen that confer improved viral fitness, resulting in several variants of interest (VOI) and variants of concern (VOC), such as the Beta, Delta, Lambda and Omicron variants (Lupala et al. 2022). Each mutation has had to be investigated computationally to find small molecules that putatively bind specifically or selectively to this viral spike/ACE2 protein-protein complex or that bind to the complex from several VOC. It is well known that the surface ACE2 receptor protein is the primary host factor recognized and targeted by SARS-CoV-2 virions (NCATS, 2020). Binding between the SARS-CoV-2 spike protein and the host ACE2 initiates binding of the viral capsid and eventually leads to viral entry in host cells, which could be disrupted when conformational changes within the angiotensin II site prevent recognition of the viral spike by the host ACE2 receptor protein (Wrobel, 2023; Yesudhas et al. 2021). This has been evidenced by MD simulations (Barros et al., 2021; Istifli et al., 2022). As an example, Barros et al. conducted an explicitly solvated, all-atom, MD simulations of the glycosylated, full-length, membrane-bound ACE2 receptor in both an apo and spike RBD-bound states and succeeded in demonstrating that mechanical contribution of the host receptor toward large spike conformational changes are required for viral cell fusion to occur (Barros et al., 2021). Thus, disruption of the spike protein/ACE2 interaction may hinder SARS-CoV-2 virions from infecting host cells (Bejoy et al., 2023; Li et al., 2023).

Natural products (NPs) have been a wonderful source of lead compounds for drug discovery and over the past four years several promising leads against coronavirus have been identified (Ebob et al. 2021; Omrani et al., 2021; Saied et al., 2021). NPs are well known to be an invaluable source of drugs and lead compounds for new therapeutic development across human diseases (Newman and Cragg, 2020). They have played a significant role in anti-infective research including both chemical biology and drug discovery (Lam, 2007; Newman and Cragg, 2009; Shu, 1998). For instance, the discovery in the 1940s of numerous penicillin-derived compounds dramatically changed the course of medical history and ushered in the antibiotic era (Roche et al., 2019; Kayser et al., 2003). Over the ensuing 60+ years, numerous other anti-infective agents (e.g. erythromycin, cephalosporin) have been discovered from nature. These NPs and various semisynthetic derivatives not only served as drugs but also as chemical probes that were used for explorations into fundamental molecular mechanisms of action. Outcomes from chemical probe research projects with NPs have been revolutionary, with improved and critical understandings of cell and pathogen biology with subsequent downstream impacts on drug development and translation. The recent global viral pandemic brought about by SARS-CoV-2 has prompted natural product researchers from around the world to investigate the natural world for new drugs, leads and chemical probes for this devastating viral infection. Several promising hit/lead and/or chemical probes have subsequently been discovered against SARS, the details of which appear in numerous reviews and primary research articles (Raimundo E Silva et al., 2021; Aggarwal et al., 2023; Chhetri et al., 2022). Continuing studies on antiviral NPs will no doubt lead to successful therapeutic outcomes in the future.

Our interest has been to investigate NPs capable of blocking viral transmission by selectively preventing the binding of the SARS-CoV-2 viral spike and the human ACE2 receptor *in vitro*. Our previous work combining the Davis Open Access Natural Product-Derived Library with new biochemical and cell-based assays to assess SARS-CoV-2 activity led to the discovery of the stilbenoid tetramers, hopeaphenol (**1**), vaticanol B (**2**) and vatalbinoside A (**3**), which are all derivatives of resveratrol (**8**) (Zulfiqar et al. 2017; Kumar et al. 2020; Tietjen et al. 2021), Fig. 1. These and other stilbenoids have been isolated from multiple plant sources including species of *Hopea*, *Vitis*, *Shorea*, *Anisoptera*, and *Vatica* species (Abe et al. 2011; Tanaka et al. 2000; Rivière et al. 2012; Nassiri-Asl and Hosseinzadeh, 2016; Ito et al. 2000; Guo et al. 2020; Davis et al. 2014; Wu et al. 2019). Compound **9** is the known neolignan with IUPAC name: 9,9'-dihydroxy-3,4-methylenedioxy-3'-methoxy[7-*O*-4',8–5'] neolignan, previously identified from the dried leaves of the plant species *Taiwania cryptomerioides* (Lin et al., 1999), henceforth also referred to simply as compound A.

Using an AlphaScreen-based method to monitor the binding of the receptor binding domain (RBD) of viral spike protein to the host ACE2 entry receptor, we observed that compounds **1–3**, but not compound **8**, could inhibit this interaction with respective half-maximal inhibitory concentrations (IC_{50} values) of 0.11, 0.067, and 0.24 μM, with > 90-fold selectivity over disruption of an unrelated ligand-receptor interaction (PD-1/PD-L1; Tietjen et al. 2021). Importantly, compounds **1–3**, but not compound **4**, could also inhibit SARS-CoV-2 replication *in vitro*, with respective half-maximal effective concentrations (EC_{50} values) of 10.2, 37.0 and 13.8 μM, compared to an EC_{50} of 2.5 μM for control inhibitor remdesivir, as well as similar antiviral activities against the Alpha and Beta VOC (Tietjen et al. 2021). While these data support stilbenoids and their derivatives as new NP-based leads to inhibit SARS-CoV-2 entry and replication across multiple VOC, the mechanisms by which these compounds dock with spike and/or ACE2, as well as whether they retain activity against more recent variants like Delta or Omicron, are not reported. To gain insights into the binding of the natural polyphenolic compounds **1**–**3**, we embarked on an *in silico* docking studies using the well-refined protein crystal structure (PDB ID: 6M0J, refinement = 2.45 Å) (Lan et al. 2020). Five theoretical fragments (**5**–**7**) and the neolignan (**9**) were also included in these studies since we were curious to know whether the large and complex molecular framework associated with compounds **1**–**3** was required for the biological activity. Identification of promising fragments was forecast to guide future natural product isolation efforts but was also identified as a means by which to guide further synthetic and medicinal chemistry efforts.

There are several reported docking sites in the SARS-CoV-2 viral spike/ACE2 protein-protein complex in the literature (Figs. 2 and 3), including the groove of dynamic residues at the interactive (recognition) surface between the receptor binding domain (RBD) that constitutes the interface between the viral spike and the human ACE2 protein, where most of the mutations are reported (Williams-Noonan et al. in 2021), as well as the angiotensin 2 binding site situated in the interior of the ACE2 receptor (Figs, 2 and 3, Lan et al. 2020).

It has been reported that compounds that bind putatively to the angiotensin 2 binding site are capable of distorting recognition of the viral spike by the ACE2 protein, hence preventing transmission of the viral or viral entry into the host cells (Fig. 3, Arya et al. 2021; Jackson et al. 2022). Since this interaction is not present in PD-1 nor PD-L1, this could potentially account for the binding selectivity observed for stilbenoids.

As an example, previous work had aimed at determining the effect that a distal active site-bound MLN inhibitor of ACE2 would have on modulating the conformation of the ACE2 N-terminal helices

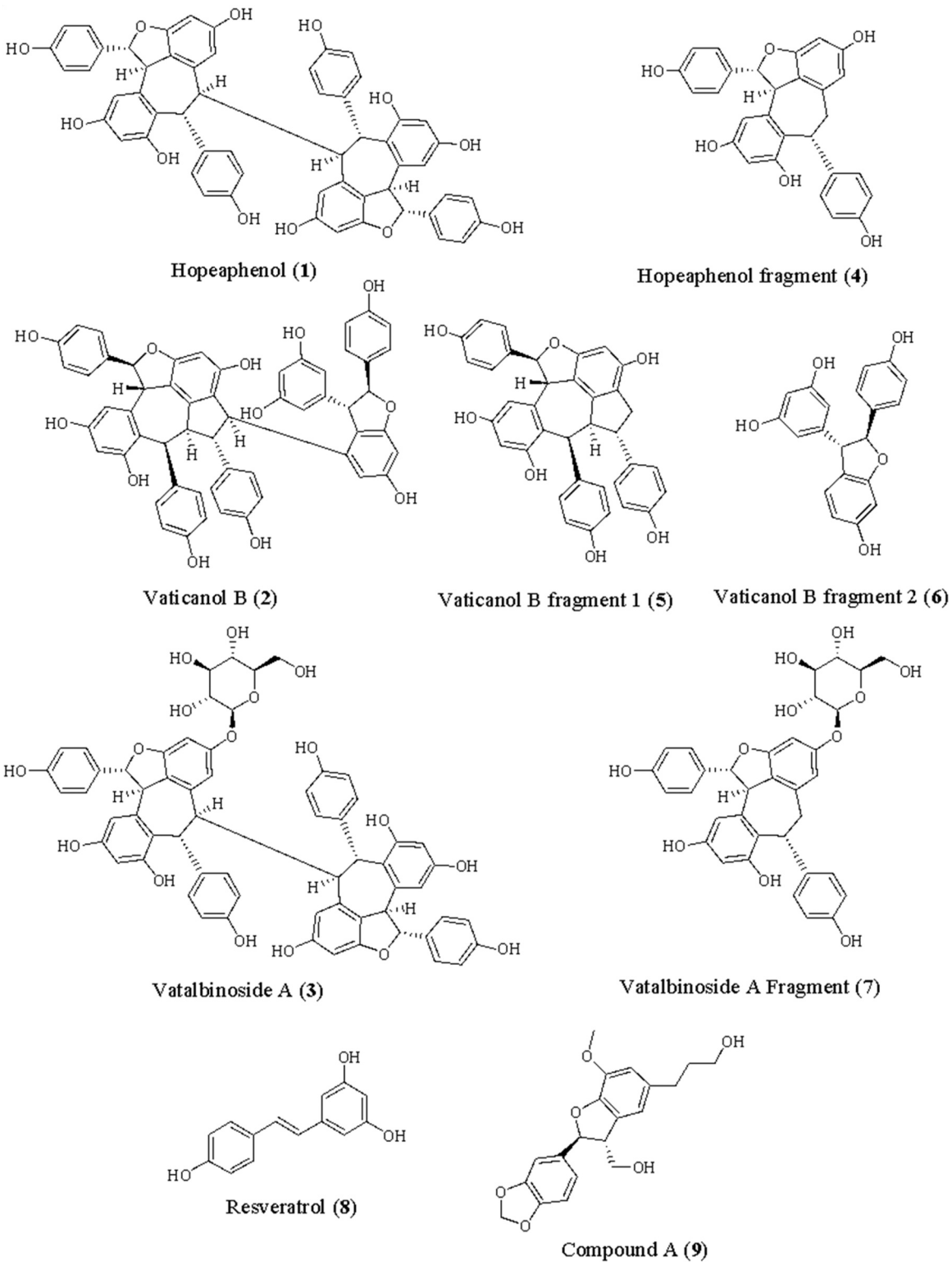

Fig. 1. Ligands used in the small molecule database for the *in silico* studies.

(Williams-Noonan et al., 2021), which led to the identification of the s-protein binding site, thus affecting the binding between ACE2 and the SARS-CoV-2 spike. In another study, several small molecules were docked into diverse sites in the complex, including the ACE2 site, followed by MD simulations to verify the stability of the docked poses (García-Iriepa et al. 2020). The authors measured the force required to pull the s-protein from ACE2 in the presence of and in the absence of small molecules bound to ACE2 s-protein binding site. This showed that the unbinding free energy from MD simulations was higher in the absence of a small molecule bound to the ACE2 binding site, demonstrating that the ACE2 binding site was a putative docking site for virtual screening studies.

In this work, we present results from the *in silico* investigation of NPs and their theoretical fragments that were recently tested *in vitro*. We have employed a panel of computational methods, including molecular docking, per-residue interaction energy decomposition with the protein

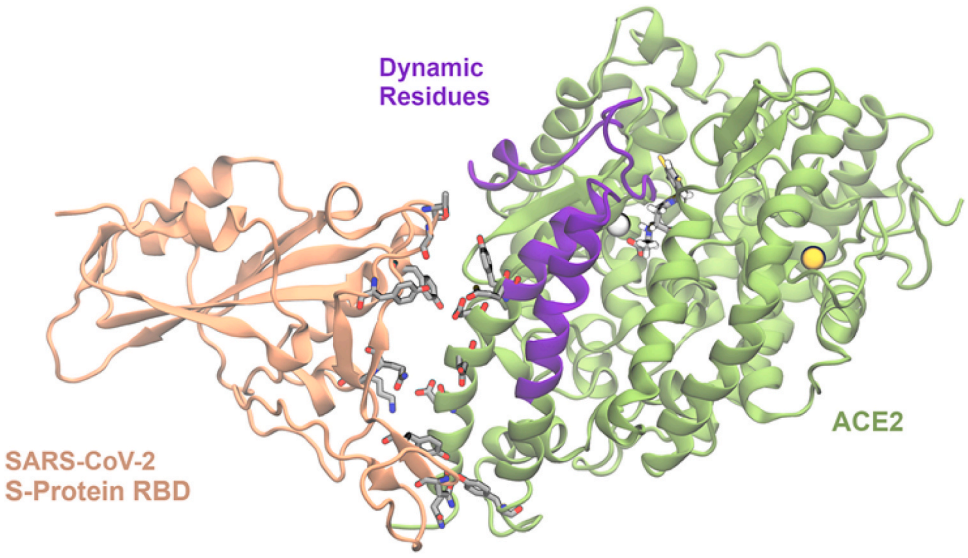

Fig. 2. Crystal Structure of ACE2-RBD-spike protein (6M0J) showing the viral entry of the spike into the human system by binding to the human ACE2 at the Spike ACE2 RBD. The amino acid residues of the groove and those of the angiotensin II site are shown in stick representation (Williams-Noonan et al., 2021).

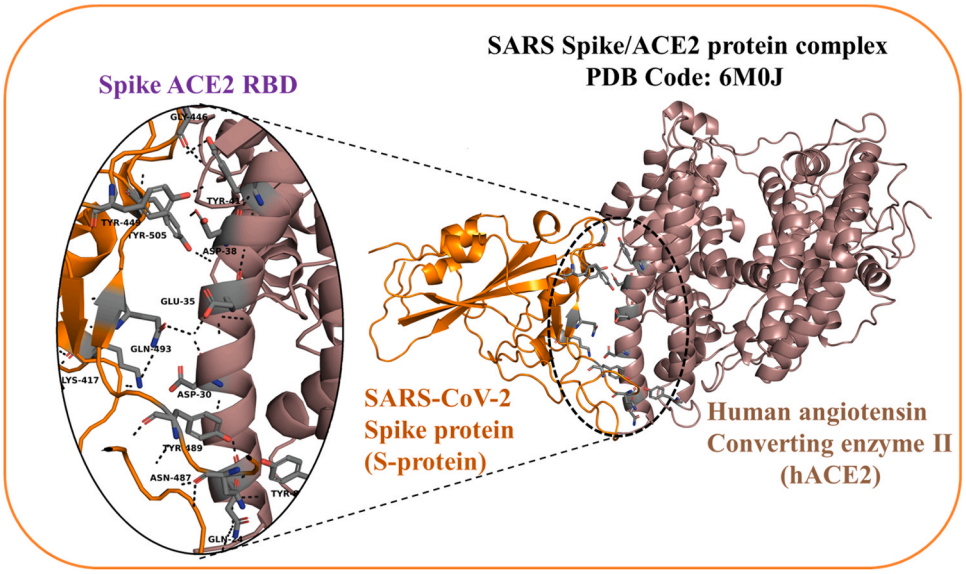

Fig. 3. Crystal Structure of ACE2-RBD-spike protein (6M0J) showing the viral entry of the spike into the human system by binding to the hACE2 at the Spike ACE2 RBD. The amino acid residues of the groove region are magnified.

target, molecular docking and binding-free energy calculations, including solvation models in an attempt to explain the observed biological activities and selectivities towards a human protein-protein complex. We have also provided insights into the potential offuture medicinal chemistry investigations on the stilbenoid-based NP fragments and derivatives.

2. Material and methods

2.1. Molecular docking procedure

A summary of the computational docking protocol/workflow has been shown in Fig. 4.

2.1.1. Protein preparation

The crystal structures of spike/ACE2 complex of SARS-CoV-2 (PDB ID: 6M0J, Lan et al. 2020) which is the Wuhan variant, along with the human PD-1/PD_L1 (PDB ID: 4ZQK) were downloaded from the Protein Data Bank (PDB; www.rcsb.org) (Berman et al. 2000; Burley et al. 2017; Burley et al. 2018). MOE software was used to delete all water molecules (Chemical Computing Group, 2016). Furthermore, Protein Preparation Wizard of Schrödinger software was used for further preparation of the protein (Schrödinger, 2017; Madhavi et al., 2013). At this stage, bond orders were assigned, and hydrogen atoms added, missing side chains were filled using the PRIME tool incorporated in the Maestro package, and the H-bond network was subsequently optimised. The protonation states at pH=7.0 were predicted using the Epik-tool in the Maestro package commercialised by Schrödinger (Schrödinger, 2017; Shelley et al., 2007). The structures were finally subjected to a restrained energy minimization step, in which the root mean square deviation (RMSD) of the atom displacement for terminating the minimization was 0.3 Å, using the OPLS2005 force field (Banks et al., 2005).

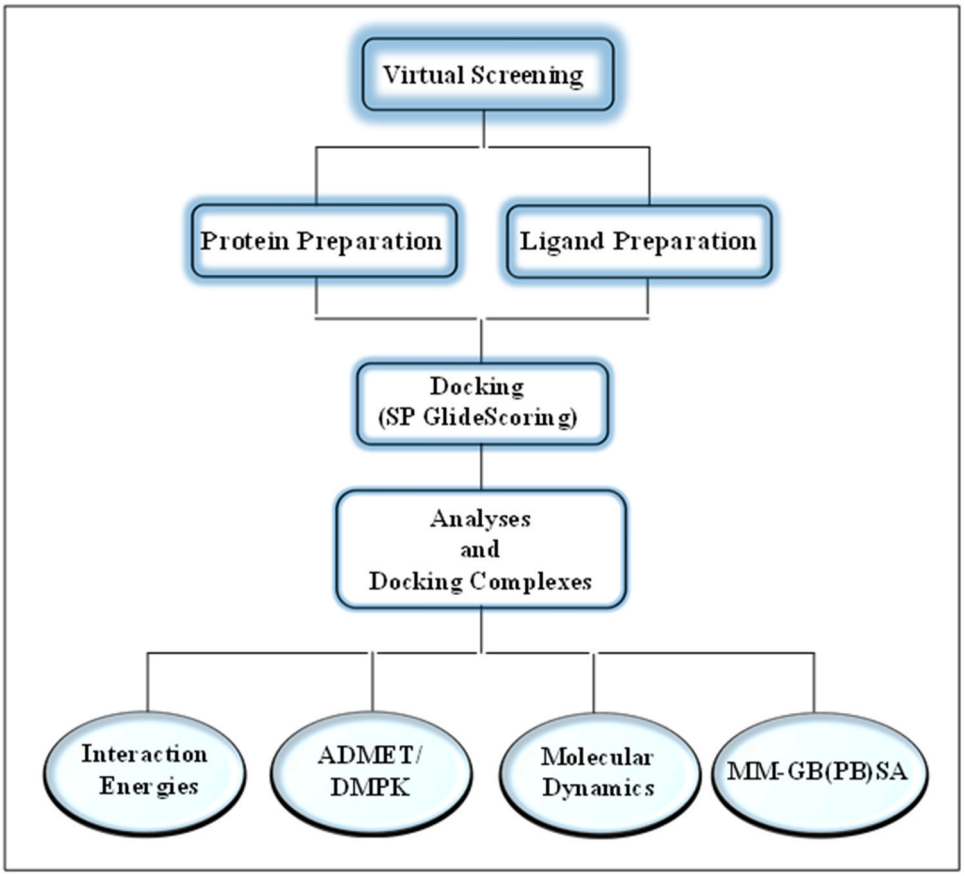

Fig. 4. Summary of computational workflow.

2.1.2. *Ligand preparation*

The 3D structures of the fragments and for the natural polyphenolic compounds **1**–**3** (Fig. 1) were generated, using Molecular Operating Environment (MOE, Chemical Computing Group, 2016). All compounds were minimised using MMFF94 force field (Halgren, 1999) prior to docking studies towards the angiotensin 2 binding site. After molecular docking, the results were extracted and selected descriptors were computed using MOE (Chemical Computing Group, 2016) to characterise the nature of each docked compound (or fragment) and the nature of each docking site and qualitatively explain binding and/or selectivity towards a specific docking site (Table 1). The ligands were then prepared for docking using the LigPrep tool (Release version 2017–2), as implemented in Schrödinger's software, where all possible tautomeric forms were generated. They were subsequently energy-minimised using the integrated Optimised Potentials for Liquid Simulations (OPLS, 2005) force field (Banks et al., 2005). Finally, ConfGen was used to calculate 60 conformers of the prepared ligands using the default settings and allowing minimization of the output conformations (S. Release, 2017–2; Watts et al., 2010).

2.2. *Docking towards the SARS-CoV-2 spike RBD/ACE2 and the human PD1/PD-L1*

Molecular docking procedures were performed using similar

Table 1
Biological activities and computed descriptors of SARS-CoV-2 spike/ACE2.

Ligands	[a]IC_{50} (μM) spike/ACE2	[b]IC_{50} (μM) PD1/PD-L1	[c]SI	[d]$LogP_{o/w}$	[e]TPSA (Å^2)	[f]Vol (Å^3)	[g]E_{ele} spike/ACE2 (kcal/mol)	[h]E_{ele} PD1/PD-L1 (kcal/mol)
1	0.110	28.300	257.27	10.9	185.9	812.3	-19.16	-20.58
2	0.067	16.600	247.76	10.9	185.9	816.1	-23.39	-26.86
3	0.240	22.300	92.92	8.6	245.2	946.3	14.50	-7.49
4	ND[i]	ND[i]	ND[i]	5.7	110.0	414.0	-37.20	-36.40
5	ND[i]	ND[i]	ND[i]	6.9	130.6	529.2	-45.00	-43.00
6	ND[i]	ND[i]	ND[i]	4.2	90.1	310.5	-31.90	-29.10
7	ND[i]	ND[i]	ND[i]	3.5	189.5	547.4	23.60	18.80
8	inactive	ND[i]	ND[i]	3.7	60.7	222.9	-31.70	-32.00
9	ND[i]	ND[i]	ND[i]	2.3	88.4	316.6	9.70	6.00

[a] *In vitro* IC_{50} values derived from the AlphaScreen (Tietjen et al., 2021); [b]Inhibitory concentration against PD1/PD-L1 binding Tietjen et al., 2021); [c]Selectivity index, calculated as the ratio of the IC_{50} values derived from the AlphaScreen and the inhibitory concentration against PD1/PD-L1 binding; [d]Computed logarithm of *n*-octanol/water partition coefficient; [e]Total polar surface area; [f]Molecular volume in Å^3; [g]Electrostatic component (Coulombic term) of the total forcefield potential energy of the low energy conformation of the molecules after minimization by the MMFF94 forcefield for the viral spike/ACE2 complex; [h]Electrostatic component (Coulombic term) of the total forcefield potential energy of the low energy conformation of the molecules after minimization by the MMFF94 forcefield for the PD1/PDL1 complex; [i]Not determined.

methods as reported in our previously published papers (Simoben et al., 2021; Divsalar et al., 2020; Simoben et al., 2018). Docking procedures were performed using the Glide program in a similar way as previously demonstrated (Simoben et al., 2021; Divsalar et al., 2020; Simoben et al., 2018). At the time of the study, there was no published crystal structure for the ACE2/Spike RBD complex with a co-crystallized ligand. Our work approach in this paper was based on seminal works reported and published after extensive in silico studies and verification of the docked site. This included but was not limited to the works of García-Iriepa et al. (2020) and Williams-Noonan et al. (2021). The re-docking of the more recently published crystal structure with co-crystallized showed a RMSD value of RMSD = 1.05 Å with respect to the native ligand in the crystal structure of PDB ID: 1R4L (see Figure S1, Supplementary Data). The docking was done based on protocol adopted from previous scientific publications and confirmed in our previous publication (Majoumo-Mbe et al., 2024), which was in agreement with the previously reported works on this target (García-Iriepa et al., 2020; Williams-Noonan et al., 2021). In this work, a grid box for the SARS-CoV-2 viral protein RBD/ACE2 human receptor (PDB ID: 6M0J) and another grid box for the human protein complex PD1/PD-L1 (PDB ID: 4ZQK, Zak et al. 2015) were generated and using specific protein residues. For the ACE2/SARS-CoV-2 protein (PDB ID: 6M0J) the whole structure was explored for the generation of a grid. For this purpose, the following amino acids Asp597, Thr598, Lys516, Val321, Gln121, Lys578, Ala283, Ser91, Asn746, Gln68, Pro744, Glu518 and Thr610 were used to generate the grid around the ACE2/SARS-CoV-2 protein. On the other hand, the grid box for the PD1/PD-L1 structure was generated using the residues Phe63, Val63, Asn66, Tyr68, Glu84, Leu122, Glu136, Ile134 and Ile126; as reported in the literature (Tang and Kim, 2019). For all the generated grid boxes, the maximum ligand size was set to 36 Å. The generated 3D conformers of the prepared ligands were docked into the receptor grid files. For the docking process, default settings were used with the exception of input ring conformation as well as writing a total of 10 poses per ligand conformer from the 20 poses that were included for each ligand conformer. The GlideScore Standard Precision (SP) mode was used as the scoring function (Halgren et al., 2004).

2.2.1. Hydrogen bond distances and verification of binding modes

The protein-ligand complexes were uploaded on MOE (Chemical Computing Group, 2016) and the atomic distances between ligand atoms and interacting protein atoms were calculated for each ligand. These were summarized in a table, to use these to explain the affinities between proteins and ligands.

2.2.2. Determination of per residue interactions of docked poses

The interaction energy (E_{int}) values were computed using the Discovery Studio (BIOVIA, 2021), following our previously reported procedure (Bekono et al. 2021). This consists of computing the (non-bonded) van der Waals and electrostatic interactions between each of the protein binding site amino acid residues and each inhibitor, using the cff forcefield. The breakdown of E_{int} into the contributions by active site residues reveals the significance of individual interactions and permits us to conduct a comparative analysis. This approach helps in the identification of affinity values which would enhance the prediction of favourable and unfavourable substitutions on the scaffold of the identified hits.

2.2.3. ADMET prediction calculations

The ADMET prediction for the NPs and their theoretical fragments was conducted using the SwissADME web server (Daina et al., 2017). Compound structures were converted to simple molecular input line entriy systems (SMILES) strings and uploaded on the SwissADME web server platform (http://www.swissadme.ch) and used to compute 46 descriptors that are often used to predict drug metabolism and pharmacokinetic profiles of druglike molecules. Some of the descriptors include molecular weight, number of rotatable bonds, molar refractivity, solubility, blood-brain-barrier permeability, gastro-intestinal absorption, P-glycoprotein binding, cytochrome inhibition, skin permeability, Lipinski violations, Veber violations, Ghose violations, Egan violations, Muegge violations, Bioavailability score, PAINS alerts, Leadlikeness violations, synthetic accessibility, etc. Additional DMPK-related parameters were computed using the QikProp tool implemented in Maestro (Schrodinger, 2017) and using the pkCSM web server (Pires et al., 2015). The additional parameters include the number of predicted metabolic reactions (#metab), predicted binding to plasma proteins like human serum albumin, HERG channel inhibition, Caco2 permeability, human intestinal absorption, skin permeability, steady-state volume of distribution, blood−brain barrier permeability, CNS Permeability, total clearance, and toxicity parameters like maximum recommended tolerated dose (MRTD), oral rat acute toxicity (LD_{50}), oral rat chronic, lowest observed adverse effect (LOAEL), as well as toxicity against fish species *Tetrahymena pyriformis* and flathead minnow toxicity (LC_{50}). The significance of the computed values will be discussed in the Results section.

2.2.4. Molecular dynamics procedure

MD systems were generated and simulated using Amber22 and AmberTools2023 (Case et al., 2023). For this study, the selected binding pose for each compound (see Results and Discussion) and the prepared protein structure from Docking with Glide were used to prepare their respective starting trajectory for MD simulation using the following steps. In step 1, the antechamber module was used to prepare the topologies and force field parameters of the respective ligands. At this step, the general Amber Force Field version 2 (GAFF2), AM1-BCC as the atomic charges method semi-empirical (AM1) and bond charge correction (BCC) were used (Jakalian et al., 2000). In step 2, The TLeaP package, the ff14SB force field for protein (Maier et al., 2015) and GAFF2 for the ligands were used to generate the various MD Systems. The generated systems were then neutralised and the TIP3P solvation model was used to solvate the systems in an octahedral box with 10 Å from the protein. In step 3, The prepared systems were used to run the MD simulation as follows. Firstly, a two-step minimization of 4000 iterations (first 3000 steepest descent and 1000 conjugate gradient) with the ligand and protein held in their initial coordinates using a force constant of 10 kcal $mol^{-1}Å^{-1}$. This was done to remove steric clashes between the solvent molecules and ions used to neutralise the system. Secondly, a second minimization of 4000 iterations (consisting of 2000 steepest descent followed by 2000 conjugate gradient) involving the whole system (solvents, ions, protein and ligand) was performed. This was subsequently followed by the third step which involved the heating of the systems from 0 K to 300 K through 100 ps MD while restraining the atoms of the protein and ligand (with a force constant of 10 kcal $mol^{-1}Å^{-1}$) to prevent the large structural deviation. Fourthly, a density evaluation during 100 ps MD was performed for the system. Afterward, the systems were equilibrated through 5 ns MD before the final 100 ns MD simulation step. The SHAKE algorithm was used to restrain all bonds involving hydrogens. At the same time, the temperature of the different systems was controlled by Langevin Dynamics using a collision frequency of 2 ps^{-1} and pressure of 1 bar. The trajectories were analysed using the CPPTRAJ module and VMD software (Roe & Cheatham III, 2013; Humphrey et al., 1996).

2.2.5. Rescoring selected stable complexes from MD by MM-GBSA

The precision of docking and scoring is often enhanced when docking poses are often rescored using more advanced methods like solvation free energies (ΔG_{solv}), including binding free energy ($\Delta\Delta G_{bind}$) calculations that include electrostatic and van der Waals interactions in a solvent (Ntie-Kang et al., 2014). A Generalized Born (GB) implicit solvent model, named GBNSR6 implemented in AmberTools (Amber 2023) that seems to be faster and more accurate than the previously published GB and Poisson Boltzmann (PB) approaches was used. GBNSR6 is an

accurate yet efficient grid-based surface GB model that is currently available in AmberTools as a stand-alone application (Forouzesh et al., 2017; Case et al., 2023). GBNSR6 calculates the solvation free energy of an input structure on a single snapshot. The method showed a good compromise between the speed and accuracy of computing polar components of the solvation free energies (ΔG_{pol}) and binding free energies ($\Delta\Delta G_{pol}$). The model tolerates a relatively coarse grid size $h = 0.5$ Å, where the grid artifact error in computing $\Delta\Delta G_{pol}$ remains in the range of $k_BT \sim 0.6$ kcal/mol. The model's estimated $\Delta\Delta G_{pol}$ values were well correlated ($r^2 = 0.97$) with the numerical Poisson–Boltzmann reference while showing virtually no systematic bias and RMSE = 1.43 kcal/mol). In AmberTools23, GBNSR6 has been integrated into MMPBSA.py such that it runs over multiple snapshots extracted from the trajectories of protein, ligand, and complex structures. To run this model, "igb = 66" is now available in MMPBSA.py.

3. Results and discussion

3.1. Database of structures docked

The 2D structure of the generated ligands is seen in Fig. 1, with biological activities shown on Table 1. Compound **2** is the most active of the stilbenoids, twice as active as compound **1**, and 4 times more active than compound **3**. All three compounds showed a hundred-fold selectivity towards the PD1/PD-L1 human protein-protein complex *in vitro* (Tietjen et al., 2021).

3.1.1. Docking results and physicochemical characterization of the compounds and docking sites

The biological activities and selected physicochemical properties of the NPs (**1**–**3**) and theoretical fragments have been summarised on Table 1. Fragments, which are all theoretically derived from the NPs (**1**–**3**), include hopeaphenol fragment (**4**), vaticanol B fragment 1 (**5**), vaticanol B fragment 2 (**6**), vatalbinoside A fragment (**7**) and resveratrol (**8**), the naturally occurring precursor of the stilbenoids. Table 2 shows the computed volumes of docking cavities and hydrophobicities of the target proteins, meanwhile, a summary of the observed amino acid residues that interact with the NPs and NP fragments in each of the selected docked poses have been summarised in Table 3.

The results show that the spike/ACE2 binding site is less voluminous and more hydrophobic than the PD1/PD-L1 site (Table 2). This implies the more hydrophobic and less bulky NPs are going to prefer the former binding site to the latter. This could explain why compounds **1** and **2**, which are more hydrophobic (with log $P_{o/w} = 10.9$, when compared with 8.6 for compound **3**) and less polar (with TPSA = 185.9 Å^2, when compared with 245.2 for compound **3**) are a lot more active against the spike/ACE2 target than compound **3**. An additional argument is that the molecular volumes of compounds **1** and **2** (812.3 and 816.1 Å^3, respectively) are very similar and both are less bulky than compound **3** (Vol = 946.3 Å^3). This correlates with the respective SI values which are more than two-fold that for compound 3. Lastly, by looking at the electrostatic compounds of the forcefield potential energies of the two target proteins, we observe that the E_{ele} values are a lot more negative (-19.16 kcal/mol and −23.39 kcal/mol, respectively) when compared with a positive value (+14.50 kcal/mol) for the least active and least selective compound **3**. The electrostatic and hydrophobic maps for the spike/ACE2 complex and PD1/PD-L1 are shown in the Supplementary materials (Figures S2-S5) These arguments are such that for the less voluminous spike/ACE2 docking site, the bulkier ligand **3** is the least active and least selective. The same holds for the PD1/PD-L1 site, except that the E_{ele} value is the highest (but not positive). As for the untested fragments and derivatives of fragments, in terms of computed log $P_{o/w}$ parameters, all fall outside the range of properties for the active whole NPs (**1**–**3**), the closest to these being for fragment 1 of vaticanol B (**5**), with log $P_{o/w} = 6.9$. This moiety of the most active of the tested NPs (vaticanol B) could contain the bioactive pharmacophore and could hold the premise for further medicinal chemistry transformations. This fragment also has the lowest E_{ele} components in their docking interactions towards the two investigated protein targets (-45.0 and −43.0 kcal/mol, respectively). The remaining fragments and derivatives of fragments might contain some elements of the bioactive pharmacophores of the active NPs (**1**−**3**) but might lack sufficient lipophilicity required for binding to the highly hydrophobic angiotensin II binding site in the SARS-CoV-2 spike/ACE2 complex investigated in the docking procedures.

In terms of the computed total polar surface areas (TPSA), again those of the fragments and fragment derivatives (**4**–**9**) are way out of the range for the active NPs (**1**–**3**), all being >800 Å^2. The closest are those of fragments **5** and **7** (529.2 and 547.4, respectively). This again points to the fact that fragment **5**, along with fragment **7** could be further derivatized to include fragments that increase the log $P_{o/w}$ and TPSA values to fall within the range of the active NPs and thus provide new scaffolds for further medicinal/synthetic chemistry studies for the further design of small molecule analogues to target SARS-CoV-2 viral spike/ACE2 host interactions for the discovery of next generation antiviral agents that could potentially prevent transmission.

Table 2
Computed volumes of docking cavities and hydrophobicities of the target proteins SARS-CoV-2 spike/ACE2 and PD1/PD1-L1.

Docked target protein-protein complex	Volume of docking cavity (Å^3)	Hydrophobicity
Spike/ACE2	22	12
PD1-PDL1	27	11

3.1.2. Analysis of hydrogen bond distances

Table 4. Analysis of hydrogen bond distances.

Compound name	Hydrogen bonding		
	Atom of ligand	Amino acid residue	Distance (Å)
Hopeaphenol (**1**)	O sp^2	Ser27	2.79
	O sp^2	Ala331	2.73
	O sp	Asp333	1.94
	O sp^2	Tyr368	2.02
	O sp^2	Asn376	2.05
	O sp^2	Gln385	2.36
Vaticanol B (**2**)	O sp^2	Ser27	2.81
	O sp^2	Ala331	2.81 and 2.22
	O sp	Asp 333	2.01
	O sp^2	Tyr368	2.00
	O sp^2	Asn376	2.02
	O sp^2	Gln385	2.30
	O sp	Arg497	2.77
Vatalbinoside (**3**)	O sp^2	Asn34	2.37
	O sp^2	Ala331	2.19 and 2.42
	O sp^2	Gln381	1.80
Hopeaphenol fragment (**4**)	O sp^2	Asn33	1.73
	O sp^2	Asp364	1.49
Vaticanol B fragment 1 (**5**)	O sp^2	Ala330	2.19
	O sp^2	Glu357	2.65
	O sp^2	Glu380	1.75
	O sp^2	His383	2.60
	O sp^2	Glu384	2.23
Vaticanol B fragment 2 (**6**)	O sp^2	Ala330	2.02
	O sp^2	Glu357	2.73
	O sp^2	Asp364	1.52
	O sp	Asn376	2.78

(*continued on next page*)

Table 3
Summary of amino acid residues of both SARS-CoV-2 spike/ACE2 complex and PD1/PD-L1 human protein interacting with the docking NPs and fragments in the selected docking poses.

Ligands	Hopeaphenol (**1**)	Vaticanol B (**2**)	Vatalbinoside A (**3**)	Compound A (**9**)
Ser25		■		
Ser26	■		■	■
Ser29				
Ala330		■		■
Trp331				■
Asp332	■		■	■
His360	■	■		
Asp364		■		
Phe372				
Arg375			■	■
Asn376	■		■	■
Glu380		■		
His383				■
Glu384	■		■	
Thr392				
Arg496			■	
PD1/PD-L1 Interactive Residues				
Glu41		■	■	
Glu43	■	■	■	■
Asp44	■	■	■	■
Val94	■	■	■	■
Arg96			■	■
Arg108		■		
Ile217			■	
Glu219	■	■	■	■
Ser220				

(*continued*)

Compound name	Hydrogen bonding		
	Atom of ligand	Amino acid residue	Distance (Å)
	O sp^2	Glu380	2.05
	O sp^2	Arg496	2.27
Valtabinoside A fragment (**7**)	O sp^2	Ser25	1.97
	O sp^2	Ser26	2.38
	O sp^2	Asp332	1.97
	O sp^2	Arg375	1.96
	O sp^2	Phe372	2.15
Compound A (**9**)	O sp^2	Ala330	2.52
	O sp^2	Glu357	2.74
	O sp^2	Asp364	1.52
	O sp	Asn376	2.89
	O sp^2	Glu380	2.07
	O sp^2	Arg496	2.37

It was observed that Asn376 appears systematically amongst the closest amino acid residues to the active compounds **1** and **2**, as well as those for fragments **6** and **9**, which could be an indicator that the design of analogues of these natural product fragments towards the spike/ACE2 target that interact closer with this residue could be worth pursuing.

3.2. *Significance of the observed selectivity in terms of ligand interactions with the respective protein targets*

From the AlphaScreen, ligands **1**–**3** were selective towards the inhibition of the spike RBD/ACE2 binding, when compared with PD1/PD-L1 binding inhibition (Tietjen et al. 2021, Table 1). A superposition of all NPs **1**–**3** has been shown in the docking sites of both proteins in Fig. 5. Interestingly, the molecular surfaces of the entire proteins (Supplementary Data: Figures S2-S5) and for the two docking sites (Figs. 6 and 7) confirmed that the spike/ACE2 surface is comparatively more hydrophobic and less polar than those of the respective unrelated PD1/PD-L1 ligand-receptor binding pair (Table 2). In Fig. 5, a superposition of docked poses of all three active NPs are shown in both docking sites. Vaticanol B is shown in cyan, while hopeaphenol is shown in green and vatalbinoside A in green. Docking studies showed that ligands and their corresponding fragments all bind between PD1 and PD-L1 where each has a particular binding mode, as shown in Fig. 5. The binding mode of each ligand results in the formation of interactions with particular amino acid residues. Table 2 revealed that the parent NPs (**1** and **3**) interact with similar residues, while the neolignan **9** interacts with completely different amino acid residues.

These ligands interact with particular residues at the PD1/PD-L1 binding site, e.g. Ser220, Glu219, Ile217, Arg108, Arg96, Val94, Asp44, Glu43 and Glu41). These interactions are missing when the fragments of the corresponding compounds are docked against this same protein. This is because all the fragments of the corresponding ligands have different docking binding modes (Fig. 8) compared with those of their parent ligand and therefore, fail to interact with the same residue as the parent ligands. This could explain the differences in activities between compound 4 and the active ligands **1**–**3**. Fig. 9 shows the difference in binding modes of the vaticanol, hopeaphenol and vatalbinoside and their corresponding fragments which are shown in brown colour.

3.2.1. *Explanation of the observed differences in activities observed in the AlphaScreens*

To further explain the observed biological activities, computational studies were performed on the spike sequence of the ancestral SARS-CoV-2 variant (i.e., Wuhan variant or "wild-type", (WT)). Docking showed that all ligands bind within the ACE2 binding/active site as depicted in Fig. 8. This observation is correlates with other studies demonstrating that ligands bind within the ACE2 binding site and therefore impose conformational changes which in turn influence the binding ability of the spike RBD with ACE2 (García-Iriepa et al., 2020; Williams-Noonan et al., 2021). Furthermore, ligands might bind and interact with ACE2 to inhibit the formation of the complex ACE2-spike protein.

Fig. 8 clearly depicts the binding mode of ligands within the ACE2 binding for the WT variant complex. Binding of the ligands is such that the interacting residues are from alpha 1 and alpha 2 (α1 and α2) N-terminal helices of the ACE2. This causes some conformational changes on the alpha-(α-) as well as the beta-(β-) interfaces of the ACE2 protein (García-Iriepa et al., 2020; Williams-Noonan et al., 2021). Analysis of the data obtained showed that vatalbinoside occupied a larger volume of 134.2 $Å^3$ compared to those of vaticanol B and hopeaphenol. This large volume tends to increase steric clashes, which decreases interaction and thus activity. Furthermore, positive log $P_{o/w}$ value implies the ligands are lipophilic though vaticanol B and hopeaphenol have higher log $P_{o/w}$ value, implying that they are more lipophilic and thus more readily dissolves in fat or lipids (lipid phase). Unlike vatalbinoside, whose structure contains a sugar moiety, makes it more hydrophilic and thus the trend of activity. Additionally, interacting residues were noted in Table 2 and the daughter fragment(s) of each parent compound were superimposed in the binding pocket. This showed that the daughter

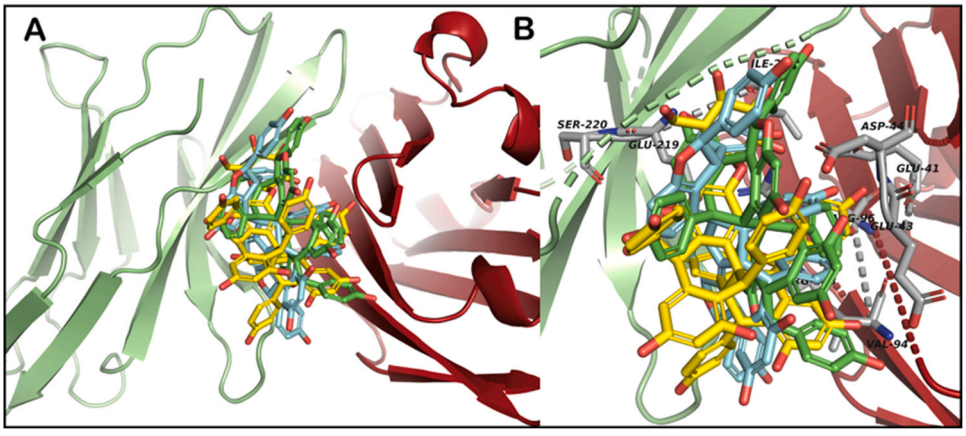

Fig. 5. Superposition of selected docking poses **(A)** showing the Receptor binding site of PD1/PD-L1 where all the stilbenoids and their corresponding fragments bind. the protein complex has PD1 in lime green, PD-L1 in red firebrick while the ligands; vaticanol B (**1**) in cyan, hopeaphenol (**2**) in green and vatalbinoside A (**3**) in yellow and each of them has a different binding pose; **(B)** a zoom-in of the binding site showing clearly interacting residues (Ser220, Glu219, Ile217, Arg108, Arg96, Val94, Asp44, Glu43 and Glu41) in grey.

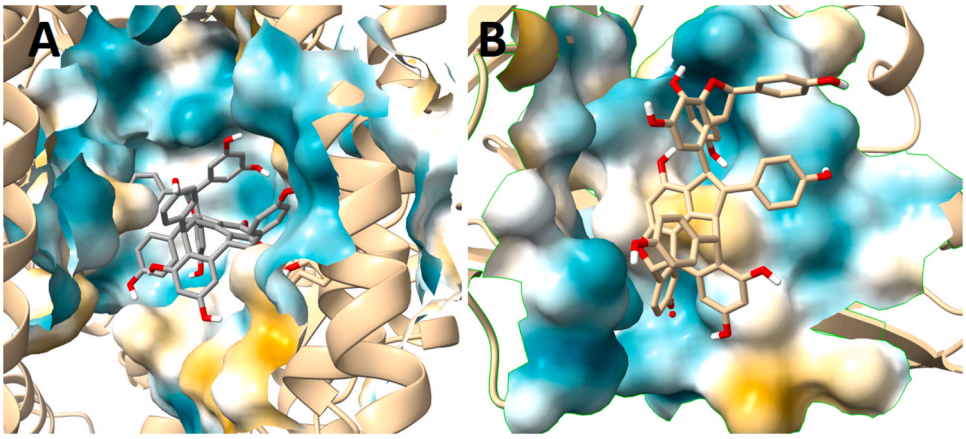

Fig. 6. Docked pose of the most active NP vaticanol B (**2**) for; (A) Spike/ACE2 and (B) PD1/PD-L1 complexes. For both structures, the protein is shown as tan cartoon secondary structure, Additionally, the dark cyan represents the most hydrophilic areas through white (neutral) to dark golden rods depicting the most hydrophobic regions. The hydrophobic surfaces of both proteins are cast in the background.

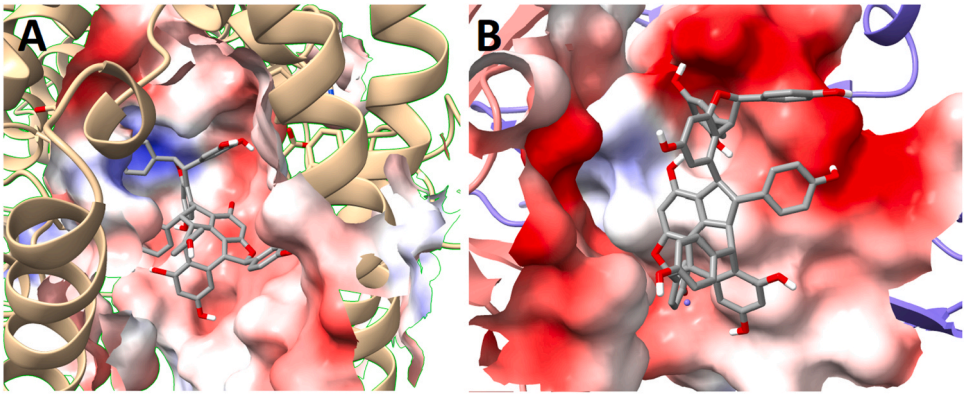

Fig. 7. Docked pose of the most active NP vaticanol B (**2**) for; (A) ACE2/Spike RBD and (B) PD1/PD-L1 complexes. For both figures, proteins are depicted as secondary structures while the colours range from red (regions that are negatively charged) through white (neutral) to blue (shows positively charged regions). The Electrostatic map for each docking site is shown in the background, with the PD1/PD-L1 site being more polar than the spike/ACE2 site.

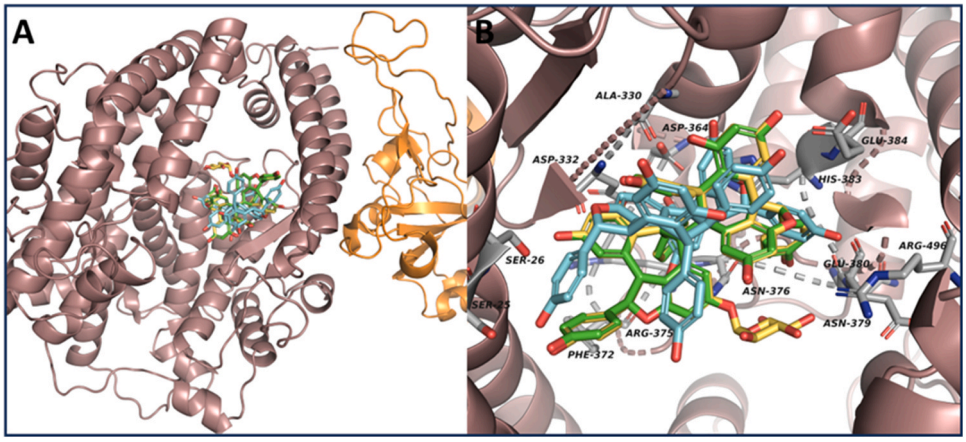

Fig. 8. (A) Superposition of all parent stibinoisde NPs showing the RBD of the Spike/ACE2 complex with the spike in orange and ACE2 in brown, respectively; (B) A zoomin of the RBD of the protein complex showing clearly the different binding poses of ligands at the ACE2 RBD with vaticanol B in cyan, hopeaphenol in green and vatalbinoside A in yellow, some interacting residues in grey.

fragments could not be superimposed on the parent compounds because they do not dock the way the parents do and hence, they adopted poses different from that of the parent compounds. Therefore, the daughter fragment(s) of each ligand does not lie well in the binding pocket which causes the required interactions with important residues not to be addressed or made and this explains why the daughter fragments would experience a decrease in activity, when compared to that of the parent compounds (Fig. 9).

A breakdown of interaction energies and per residue interactions is shown on Table 4. The results revealed that the lowest value of E_{int}

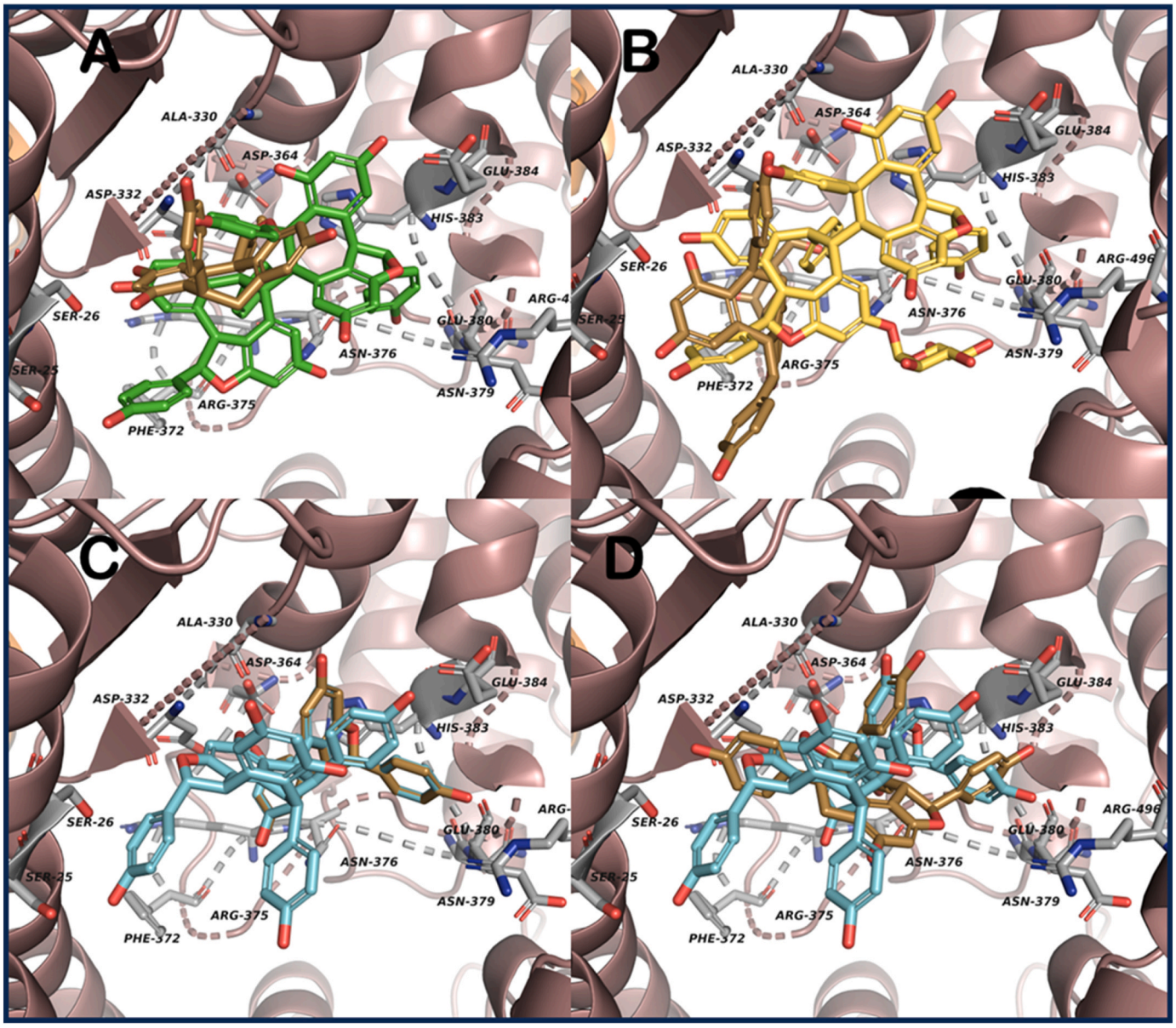

Fig. 9. Focuses on the different poses made by the different ligands superpositioned with their corresponding daughter fragments in brown. **A)** Shows hopeaphenol (green), **B)** vatalbinoside (yellow), with both C) and D) showing vaticanol B in cyan.

(15.26 kcal/mol) corresponds to compound **1** (Hopeaphenol). The corresponding value is 21603.09 kcal/mol for the most active compound Vaticanol B (**2**) and 294.12 kcal/mol for Vatalbinoside A (**3**). In all cases, the total van der Waals contributions are more significant than the electrostatic compounds, which is in agreement with the previously shown docking results, that suppose that the binding of these NPs to the ACE2 target site are driven more by van der Waals and hydrophobic interactions. For Hopeaphenol, the residue with the highest contribution towards binding to the protein target is Asn376 (with respective E_{vdW} and E_{ele} contributions of 43.53 and −2.23 kcal/mol). For Vaticanol B, the polar residues His361 and His384 make the highest interaction contributions, while for Vatalbinoside A, Asn376 and Arg377 make the highest contributions. When compared with the fragments (results shown on Table S1 to S4, Supplementary Data), we observed that the total interaction energies of the NPs are quite out of range when compared with the tested NPs, most likely due to differences in the consistent forcefield (cff) used in this calculation. Per residue analysis showed that the residues with the strongest interactions for fragment **4** were Trp331, Asp332, and Thr329. For fragment **5**, these were Trp331, Asp332 and Thr329, while the following triads (His383, Asn376, Arg496), (Phe22, Trp331, Trp51) and (Trp331, Asn376, His383) interacted best with fragments **6**, **7** and **9**, respectively. It was shown that Asn376 interacted with fragments **6** and **9** with similar per-residue interaction energies as the active NPs Hopeaphenol and Vatalbinoside A. Compound **8** was not included in the investigation as it had already been shown to be inactive the AlphaScreen.

3.2.2. *Selectivity of hopeaphenol towards the VOC*

Our screening results for these compounds showed that hopeaphenol had inhibited both the variants of concern. B.1.1.7/Alpha and B.1.351/Beta in both viral and spike-containing pseudovirus assays with similar or improved activities over the USA-WA1/2020 variant (Tietjen et al. 2021). Another related study from our group has shown that the synthetic compound 5-chloro-3-(2-(2,4-dinitrophenyl) hydrazono) indolin-2-one selectively inhibited the fusion of the viral spike/ACE2 fusion for the Wuhan strain (WT), the Beta, Delta, Lambda, and Omicron variants at concentrations of 447.5, 490.3, 464.1, 628.5, and 614.6 nM, respectively (Majoumo-Mbe et al. 2024). This selectivity between the

Table 4
Decomposition of Interaction Energies of Docked Complexes for the Biologically Active NPs.

Spike/ACE2-Hopeaphenol (**1**) Complex	E_{int}^{tot*} (kcal/mol)	E_{vdW}^{tot**} (kcal/mol)	E_{ele}^{tot***}(kcal/mol)
	15.26	24.48	-9.21
Decomposition of Interaction Energies			
Residue	E_{int}^{a} (kcal/mol)	E_{vdW}^{b} (kcal/mol)	E_{ele}^{c} (kcal/mol)
Phe23	2.34	2.55	-0.21
Ser27	-1.76	-1.23	-0.53
Thr330	-5.21	-4.47	-0.75
Ala331	-3.22	-2.84	-0.38
Trp332	-4.58	-4.11	-0.47
Asp333	-3.54	-2.56	-0.97
Tyr368	-0.86	-0.49	-0.37
Arg376	41.30	43.53	-2.23
Asn377	-3.64	-2.11	-1.53
Gly378	-0.62	-0.82	0.20
Glu385	-4.95	-2.98	-1.97
Spike/ACE2-Vaticanol B (**2**) Complex	E_{int}^{tot*} (kcal/mol)	E_{vdW}^{tot**} (kcal/mol)	E_{ele}^{tot***}(kcal/mol)
	21603.09	21607.59	-4.50
Decomposition of Interaction Energies			
Residue	E_{int}^{a} (kcal/mol)	E_{vdW}^{b} (kcal/mol)	E_{ele}^{c} (kcal/mol)
Ser30	1.53	2.17	-0.64
Asn34	-3.14	-2.16	-0.98
Ala331	-4.93	-3.52	-1.40
Trp332	-5.22	-5.23	0.00
His361	228.67	229.26	-0.59
Glu381	-1.49	-0.53	-0.96
His384	21387.66	21387.59	0.07
Spike/ACE2-Vatalbinoside A (**3**) Complex	E_{int}^{tot*} (kcal/mol)	E_{vdW}^{tot**} (kcal/mol)	E_{ele}^{tot***}(kcal/mol)
	294.12	308.86	-14.74
Decomposition of Interaction Energies			
Residue	E_{int}^{a} (kcal/mol)	E_{vdW}^{b} (kcal/mol)	E_{ele}^{c} (kcal/mol)
Phe23	7.01	7.18	-0.17
Ser27	-1.73	-1.25	-0.48
Trp52	-1.29	-1.16	-0.13
Thr330	-5.07	-4.32	-0.75
Ala331	-3.78	-3.10	-0.68
Trp332	-4.46	-4.08	-0.38
Asp333	-3.80	-3.01	-0.79
Tyr368	-0.93	-0.50	-0.44
Arg376	42.38	44.67	-2.28
Asn377	274.73	280.09	-5.36
Gly378	0.33	-0.50	0.83
Glu385	-4.54	-2.89	-1.65
Arg497	-4.75	-2.29	-2.46

E_{int}^{tot*} = total interaction energy in kcal/mol); E_{vdW}^{tot**} van der Waals contribution to the total interaction energy in kcal/mol; E_{ele}^{tot***} = electrostatic contribution to the total interaction energy in kcal/mol; E_{int}^{a} = contribution to the total interaction energy per residue in kcal/mol; E_{vdW}^{b} = van der Waals contribution to the total interaction energy per residue in kcal/mol; E_{ele}^{c} = electrostatic contribution to the total interaction energy per residue in kcal/mol.

various strains could be explained based on drug-target interactions within the angiotensin II binding site.

3.2.3. ADME/T prediction analysis

The prediction of ADME properties have been summarised on Table 5, with additional DMPK and toxicity predictions included on Table 6. Results show the main physicochemical properties often used to predict the absorption, distribution, metabolism, excretion, and toxicity profiles of drug molecules. We observed that, although the NPs **1**–**3** have sub-micromolar IC_{50} values for blocking the spike/ACE fusion in the AlphaScreens, they have no drug-like properties (they all violate Lipinski's "Rule of Five" (Ro5) and all violate Veber and Lead-likeness criteria), meaning that they cannot be considered as drugs-like molecules. Although drug-likeness is often seen as an essential criterion for candidate selection for drug development for determination to decide which molecules should become oral drugs (Vistoli et al. 2008; Ursu et al. 2011), a more important consideration for molecules that target the blocking of viral transmission would rather be skin permeability (log k_p) and blockage of binding to p-glycoproteins (Pgp). Besides, all three molecules show poor solubility profiles, have poor bioavailabilities and have very high synthetic accessibility scores. Amongst the promising theoretical fragments (**5** and **7**), these show poor to moderate solubilities, none bind to Pgp, and have log k_p values within the same range as the parent compounds (**1**–**3**), thus suggesting the theoretical fragments **5** and **7** for further medicinal chemistry.

From Table 6 we observe that the NPs (**1**–**3**) have much poorer predicted ADMET and DMPK profiles when compared with the fragments. Obviously the NPs are not drug-like. Fragments **6**, **8** and **9** showed #star prediction of 0, indication that all the 64 QikProp computed parameters fell within the recommended range for 95% of known drugs. The #star had been previously shown as a nice criterion for deciding whether to consider NPs for further medicinal chemistry modification or not (Onguéné et al., 2018). Besides, these compounds have the least number of predicted metabolic reactions (#metab) of 7, 3 and 5, respectively, when compounds with $>$ 10 metabolites for the other NPs and fragments. Although compound **8** is drug-like it had been tested negative in the AlphaScreen. Besides, the solvent-accessible surface area (SASA) parameter for fragments **6**, **8** and **9** are all $<$700 Å^2 while the remaining SASA values are much higher, even two-fold in some cases. Also pkCSM predictions for fragments **6** and **9** show that CYP inhibition and hERG I blockage look promising, as well as the overall toxicity profiles of these fragments.

3.2.4. MD simulations

To further investigate the stability of the docked poses for compounds **1**–**3** in the spike/ACE2 target site, a 100 ns MD simulation was run for the holo complex as well as for the docked poses for each compound. A plot of the root-mean-square-deviations (RMSD) per MD frame and the root-mean-square-fluctuations (RMSF) per amino acid residue for the holo ACE2/SpikeRBD complex showed that the complex was fairly stable throughout the simulation, particularly the all RMSD values were shown to be $<$4 Å and all RMSF values were $<$8 Å, the only spikes being observed between residues 600 and 640, which correspond to the docking site (Supplementary Data: Figure S6). In the presence of docked hopeaphenol (**1**), the protein-ligand complex shows good stability (Fig. 10), a similar observation with docked vaticanol B (**2**) (Supplementary Data: Figure S7) and docked vatalbinoside (**3**) (Supplementary Data: Figure S8).

Fig. 11 shows a plot of the stability of all the docked complexes including the compounds **1**–**3** superimposed with that of the holo (undocked) spike/ACE2 protein-protein complex. It is observed that the highest fluctuations are again shown for the residues between residues 600 and 640 for the holo protein. This drops significantly in the presence of the docked ligands, the lowest RMSD values being observed for this region for the most active vaticanol B (**2**) ligand. There was no marked difference in RMSF curves between the fluctuation curves for hopeaphemnol (**1**) and vatalbinoside A (**3**) for this region (Fig. 11).

3.2.5. MM-GBSA binding free energy analyses

Binding energy values of NPs and fragments inhibitors against spike/ACE2, computed using the MM-GBSA approach (in kcal mol^{-1}) have been tabulated on Table 7, along with the electrostatic, van der Waals and surface tension components.

The ΔG_{solv} (solvation term of the binding free energy for the protein-ligand complex) and the enthalpy term in the gas phase (ΔG_{gas}) from the MM-GBSA model shows that the NPs (**1**–**3**) lie in close range with those of the fragment **6** (a fragment of vaticanol B, the most active of the three NPs). The affinities of compounds **8** and **9** seem to have moderate

Table 5
Summary of ADME profiles of NPs and their fragments and fragment derivatives from SwissADME. Additional descriptors have been included in the Supplementary Data (Table S1).

Ligands	MW (Da)[a]	NRB[b]	Lipinski Viol[c]	BBB[d]	Pgp[e]	Sol[f]	Log k_p^g	PAINS[h]	Syn Acc[i]	Bioavalability[j]	Veber Viol[k]	Leadlikeness[l]
1	906.93	5	3	No	Yes	Insoluble	-5.36	0	7.53	0.17	1	2
2	906.93	6	3	No	Yes	Insoluble	-5.36	0	7.55	0.17	1	2
3	1069.07	8	3	No	Yes	Insoluble	-7.62	0	9.02	0.17	1	3
4	454.47	2	0	No	No	Poor	-5.61	0	4.78	0.55	0	2
5	572.6	3	2	No	No	Poor	-5.46	0	5.65	0.17	0	2
6	336.34	2	0	No	Yes	Moderate	-5.87	0	3.66	0.55	0	0
7	616.61	5	3	No	No	Moderate	-7.87	0	6.41	0.17	1	1
8	228.24	2	0	Yes	No	Soluble	-5.47	0	2.02	0.55	0	1
9	344.36	5	0	No	Yes	Moderate	-7.01	0	4.00	0.55	0	0

[a] Molecular weight in Daltons; [b]Number of rotatable single bonds; [c]Number of Lipinski violations; [d]Blood-brain barrier permeability; [e]P-glycoprotein binding affinity; [f]Solubility in water; [g]Logarithm of skin permeability in (cm/s); [h]Number of pan-assay interference (PAINS) alerts; [i]Synthetic accessibility; [j]Bioavailability score; [k]Number of Veber violations; [l]Lead-likeness prediction.

Table 6
Summary of selected DMPK and toxicity profiles of NPs and their fragments and fragment derivatives from QikProp and pkCSM. The remaining parameters are available in the Supplementary materials.

Ligands	#star[a]	MDCK[b]	Caco-2[c]	logHERG[d]	CNS[e]	metab[f]	SASA[g]	VD_{ss}^h	$Frac_{ub}^i$	CYP2D6[j]	CYP3A4[k]	CYP1A2[l]
1	14	0.07	0.26	-7.74	-2	22	1072.75	0.010	0.381	No	Yes	No
2	14	0.10	0.39	-8.07	-2	21	1084.48	0.005	0.381	No	Yes	No
3	14	0.03	0.14	-7.91	-2	25	1193.99	0.010	0.381	No	Yes	No
4	1	20.03	51.46	-6.52	-2	11	703.26	-1.737	0.381	No	No	Yes
5	4	3.05	9.03	-6.99	-2	13	831.74	-0.483	0.396	No	Yes	Yes
6	0	24.33	61.61	-5.77	-2	7	586.37	-1.259	0.165	No	No	Yes
7	6	1.17	3.73	-7.29	-2	13	917.38	-1.276	0.379	No	No	No
8	0	126.54	283.26	-5.26	-2	3	476.42	-0.042	0.189	No	No	Yes
9	0	134.66	300.04	-5.49	-2	5	616.45	0.037	0.037	No	Yes	Yes
Ligands	Cl_{tot}^m	E_{Ren}^b	Tox_{AMES}°	D_{max}.[p]	hERG I[q]	hERG II[r]	Tox_{ORA} (LD_{50})[s]	Tox_{ORC} (LOAEL)[t]	Tox_{Hep}^u	SS[v]	$Tox_{T.p}^w$	Tox_{Minnow}^x
1	-3.010	No	No	0.438	No	Yes	2.482	0.865	No	No	0.285	7.155
2	-3.239	No	No	0.438	No	Yes	2.482	5.919	No	No	0.285	9.422
3	-3.221	No	No	0.438	No	Yes	2.482	10.725	No	No	0.285	17.679
4	0.081	No	No	0.348	No	Yes	2.275	2.619	Yes	No	0.285	1.637
5	0.012	No	No	0.438	No	Yes	2.463	3.290	Yes	No	0.285	1.940
6	0.095	No	Yes	0.386	No	Yes	2.351	1.736	No	Yes	0.286	1.503
7	-0.336	No	No	0.334	No	Yes	2.478	5.013	No	No	0.285	8.753
8	0.133	No	Yes	0.418	No	No	1.826	1.707	No	No	1.043	1.515
9	0.099	No	Yes	-0.029	No	Yes	1.962	1.592	No	No	0.377	1.841

[a] Overall ADME-compliance score – druglikeness parameter (indicated by #stars), which is the number of computed parameters in QikProp which fall out of the recommended range for 95% of known drugs (Recommended range is 0–3); [b]QikProp predicted apparent Madin-Darby canine kidney cell permeability in nm s^{-1} (Irvine et al., 1999) (Recommended range is < 25 poor, > 500 great); [c]QikProp predicted apparent Caco-2 cell membrane permeability, in nm s^{-1} (in Boehringer–Ingelheim scale, Yazdanian et al., 1998; Irvine et al. 1999; Stenberg et al., 2001) (Recommended range is < 5 low, > 100 high); [d]QikProp predicted IC_{50} value for blockage of HERG K^+ channels (Cavalli et al. 2002; De Ponti et al. 2001) (concern < −5); [e]Predicted CNS activity was computed on a −2 (inactive) to +2 (active) scale; [f]Number of likely metabolic reactions (Recommended range is 1–8); [g] Total solvent-accessible molecular surface, in $Å^2$ (probe radius 1.4 Å) (Recommended range is 300–1000 $Å^2$); [h]Volume of distribution in human predicted by pkCSM in log L/kg; [i]Fraction of unbound drug (human) predicted by pkCSM in fractional unit; [j]CYP2D6 inhibition by pkCSM (Yes/No); [k]CYP3A4 inhibition by pkCSM (Yes/No); [l]CYP1A2 inhibition by pkCSM (Yes/No); [m]Total predicted rate of clearance by pkCSM in log ml/min/kg; [n]Renal excretion OCT2 substrate predicted by pkCSM (Yes/No); °AMES toxicity prediction by pkCSM (Yes/No); [p]Maximum tolerated dose in humans predicted by pkCSM in log mg/kg/day; [q]predicted hERG I inhibitor by pkCSM (Yes/No); [r]predicted hERG II inhibitor by pkCSM (Yes/No); [s]predicted Oral Rat Acute Toxicity (LD_{50}) by pkCSM in mol/kg; [t]Oral Rat Chronic Toxicity predicted by pkCSM in log mg/kg_bw/day; [u]predicted pkCSM hepatotoxicity (Yes/No); [v]predicted pkCSM skin sensitisation (Yes/No); [w]*Tetrahymena pyriformis* fish species toxicity predicted by pkCSM in numeric (log μg/L); [x]Minnow fish species toxicity predicted by pkCSM in numeric (log mM).

affinities towards this protein while **4**, **5** and **7** towards the protein are much weaker. The electrostatic and van der Waals components of the gas phase binding free energies follow the same trend, suggesting that careful structural modifications of fragments **6**, **8** and **9** could lead to synthetically derived compounds from a fragment of the initially tested NPs (**1**–**3**).

4. Conclusions

Computational approaches for drug discovery, including molecular docking and MD simulations have proven track record for their ability to use interactions between protein targets and small molecules to explain structure-activity relationships (SAR) and suggest changes for the design or novel derivations of docked ligands to design synthetic analogues that would potentially show improved activities. Since NPs are often only isolated from their natural sources in significantly small quantities that would not warrant further medicinal/synthetic chemistry exploration, it is important to only use the sub-micromolar range NP inhibitors of SARS-CoV-2 spike/ACE2 fusion and their derived pharmacophores to inspire the discovery of small synthetically accessible compounds that contain the NP-pharmacophores. In this paper, we have used molecular docking and MD simulations to elucidate the binding modes of three naturally occurring compounds and explain their SAR. We have also used ADME predictions to rule out which fragments are potentially useful for further medicinal chemistry work. We suggest that a theoretical fragment from the most active NP, vaticanol B, is the most promising scaffold as it contains the relevant pharmacophores and pharmacophysical parameters for future drug discovery efforts. Exploring the current pharmacophores distances between the docked ligands and the interacting amino acid residues and the decomposition

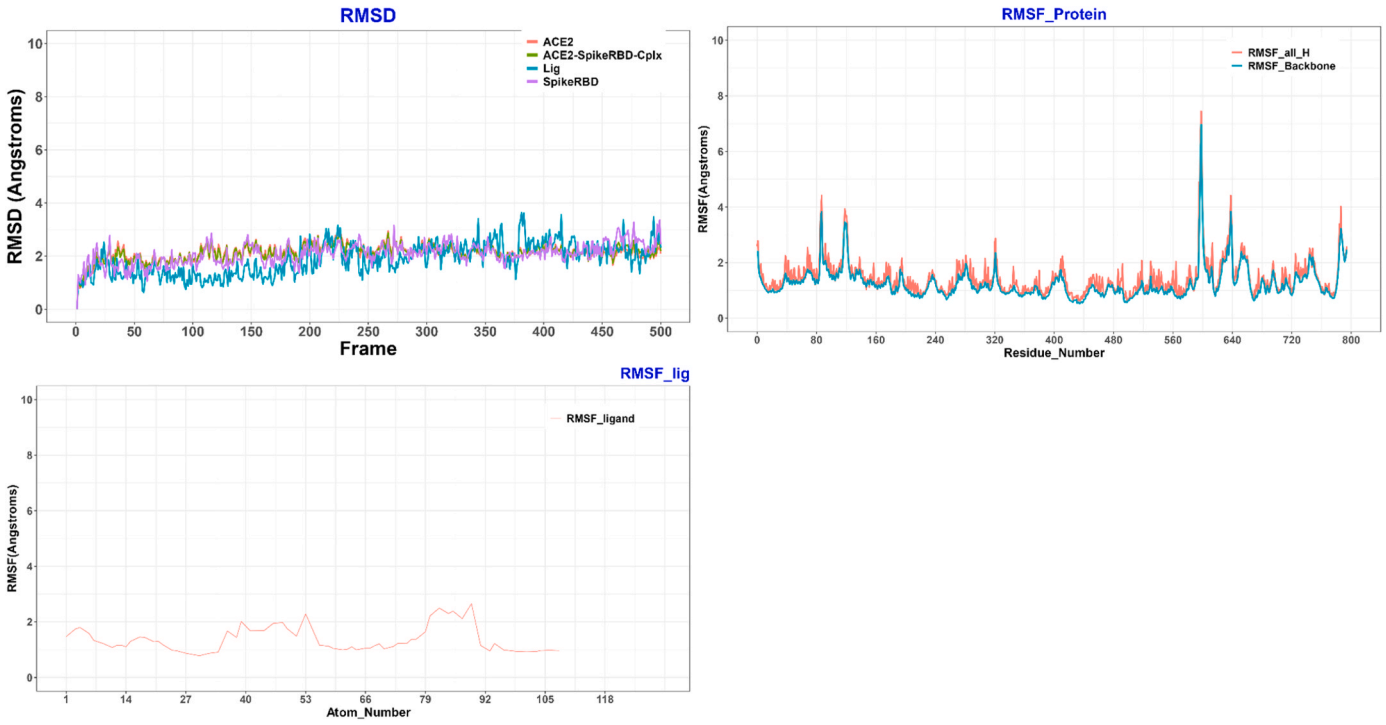

Fig. 10. (top left) RMSD for the docked hopeaphenol in ACE2/Spike RBD complex; (top right); RMSF for the docked hopeaphenol in ACE2/SpikeRBD complex; and (bottom) RMSF for the hopeaphenol Ligand -RMSF for ACE2/Spike RBD complex.

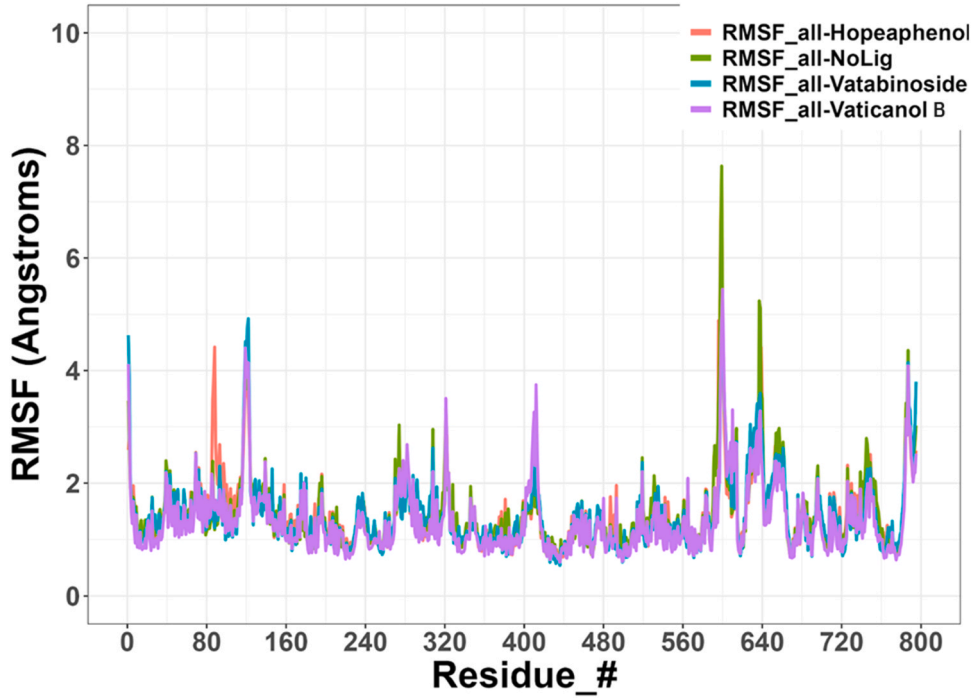

Fig. 11. Superposition of RMSF graphs per amino acid residues for the holo spike/ACE2 complex (no ligand) with those of the docked complexes with NPs (**1**–**3**).

of the total interaction energies according to the interaction amino acids show that the amino acid Asn376 appears both in the tested active compounds and the fragments **6** and **9**. The potential for virtual screening campaigns would be designed based on pharmacophores derived from the docked complexes with these fragments for the identification of novel scaffolds for the discovery novel spike/ACE2 inhibitors. Further insights for medicinal chemistry could be suggested around these scaffolds for further discovery. We suggest that small sized fragments from the fragments 6 and 9 be used starting points for the identification of drug-like NPs like from the African Natural Products Database (ANPDB, Ntie-Kang et al., 2017; Simoben et al., 2020)

Table 7
MM-GBSA binding free energies for compounds 1–9 towards spike/ACE2.

Ligand	E^{a}_{vdW}	E^{b}_{ele}	E^{c}_{surf}	ΔG^{d}_{gas}	ΔG^{e}_{solv}
1	-47.99	-80.44	-7.74	-128.44	84.71
2	-46.34	-87.27	-7.45	-133.61	89.59
3	-67.79	-93.70	-10.58	-161.49	114.48
4	-23.34	-38.68	-3.59	-62.02	45.31
5	-33.82	-52.82	-5.43	-86.63	56.18
6	-38.06	-86.81	-5.84	-124.87	80.57
7	-16.50	-6.00	-2.34	-22.49	21.85
8	-38.14	-67.62	-6.07	-105.76	71.71
9	-33.55	-68.75	-6.03	-102.30	60.61

[a]van der Waals component of the binding free energy; [b]Electrostatic component of the binding free energy; [c]Surface accessible surface area proportional to the surface tension; [d]The enthalpy term in the gas phase; [e]Solvation energy for the protein–ligand complex

CRediT authorship contribution statement

Joseph M. Salvino: Writing – review & editing, Supervision, Conceptualization. **Luis J. Montaner:** Writing – review & editing, Supervision, Project administration, Conceptualization. **Rohan A. Davis:** Writing – review & editing, Writing – original draft, Supervision, Resources, Funding acquisition, Data curation, Conceptualization. **Fidele Ntie-Kang:** Writing – review & editing, Writing – original draft, Supervision, Project administration, Funding acquisition, Data curation, Conceptualization. **Boris Davy Bekono:** Data curation, Formal analysis, Investigation, Software, Writing – original draft, Writing – review & editing. **Cyril T. Namba-Nzanguim:** Writing – review & editing, Writing – original draft, Investigation, Data curation. **Conrad V. Simoben:** Writing – review & editing, Writing – original draft, Supervision, Software, Resources, Formal analysis, Data curation. **Ian Tietjen:** Writing – review & editing, Writing – original draft, Resources, Funding acquisition, Data curation, Conceptualization. **Joel Cassel:** Writing – review & editing, Validation, Methodology, Formal analysis, Data curation.

Declaration of Competing Interest

The authors declare that they have no known competing financial interests or personal relationships that could have appeared to influence the work reported in this paper.

Data availability

No data was used for the research described in the article.

Acknowledgements

The authors acknowledge the National Health and Medical Research Council (APP1024314 to RAD), the Australian Research Council for support toward nuclear magnetic resonance (NMR) and mass spectrometry (MS) equipment (LE0668477, LE140100119, and LE0237908), and a linkage research grant (LP120200339 to RAD). We acknowledge financial support from the Bill & Melinda Gates Foundation through the Calestous Juma Science Leadership Fellowship awarded to Fidele Ntie-Kang (grant award number: INV-036848 to University of Buea). FNK also acknowledges joint funding from the Bill & Melinda Gates Foundation (award number: INV-055897) and LifeArc (grant ID: 10646) under the African Drug Discovery Accelerator program. FNK acknowledges further funding from the Alexander von Humboldt Foundation for a Research Group Linkage project.

Appendix A. Supporting information

Supplementary data associated with this article can be found in the online version at doi:10.1016/j.microb.2024.100059.

References

Abe, N., Ito, T., Oyama, M., Sawa, R., Takahashi, Y., Iinuma, M., 2011. Resveratrol derivatives from Vatica albiramis. Chem. Pharm. Bull. (Tokyo) 59 (4), 452–457. https://doi.org/10.1248/cpb.59.452.

Aggarwal, V., Bala, E., Kumar, P., Raizada, P., Singh, P., Verma, P.K., 2023. Natural products as potential therapeutic agents for SARS-CoV-2: a medicinal chemistry perspective. Curr. Top. Med Chem. 23 (17), 1664–1698. https://doi.org/10.2174/1568026623666230327125918.

Arcon, J.P., Turjanski, A.G., Martí, M.A., Forli, S., 2021. Biased docking for protein-ligand pose prediction. Methods Mol. Biol. 2266, 39–72. https://doi.org/10.1007/978-1-0716-1209-5_3.

Arya, R., Kumari, S., Pandey, B., Mistry, H., Bihani, S.C., Das, A., Prashar, V., Gupta, G. D., Panicker, L., Kumar, M., 2021. Structural insights into SARS-CoV-2 proteins. J. Mol. Biol. 433 (2), 166725 https://doi.org/10.1016/j.jmb.2020.11.024.

Baig, M.H., Ahmad, K., Roy, S., Ashraf, J.M., Adil, M., Siddiqui, M.H., Khan, S., Kamal, M.A., Provazník, I., Choi, I., 2016. Computer aided drug design: success and limitations. Curr. Pharm. Des. 22 (5), 572–581. https://doi.org/10.2174/1381612822666151125000550.

Banks, J.L., Beard, H.S., Cao, Y., Cho, A.E., Damm, W., Farid, R., Felts, A.K., Halgren, T. A., Mainz, D.T., Maple, J.R., Murphy, R., Philipp, D.M., Repasky, M.P., Zhang, L.Y., Berne, B.J., Friesner, R.A., Gallicchio, E., Levy, R.M., 2005. Integrated modeling program, applied chemical theory (IMPACT). J. Comput. Chem. 26 (16), 1752–1780. https://doi.org/10.1002/jcc.20292.

Barros, E.P., Casalino, L., Gaieb, Z., Dommer, A.C., Wang, Y., Fallon, L., Raguette, L., Belfon, K., Simmerling, C., Amaro, R.E., 2021. The flexibility of ACE2 in the context of SARS-CoV-2 infection. Biophys. J. 120 (6), 1072–1084. https://doi.org/10.1016/j.bpj.2020.10.036.

Bejoy, J., Williams, C.I., Cole, H.J., Manzoor, S., Davoodi, P., Battaile, J.I., Kaushik, A., Nikolaienko, S.I., Brelidze, T.I., Gychka, S.G., Suzuki, Y.J., 2023. Effects of spike proteins on angiotensin converting enzyme 2 (ACE2). Arch. Biochem Biophys. 748, 109769 https://doi.org/10.1016/j.abb.2023.109769.

Bekono, B.D., Ntie-Kang, F., Owono Owono, L.C., Megnassan, E., 2018. Targeting cysteine proteases from *Plasmodium falciparum*: a general overview, rational drug design and computational approaches for drug discovery. Curr. Drug Targets 19 (5), 501–526. https://doi.org/10.2174/1389450117666161221122432.

Bekono, B.D., Esmel, A.E., Dali, B., Ntie-Kang, F., Keita, M., Owono, L.C.O., Megnassan, E., 2021. Computer-aided design of peptidomimetic inhibitors of falcipain-3: QSAR and pharmacophore models. Sci. Pharm. 89 (4), 44. https://doi.org/10.3390/scipharm89040044.

Berman, H.M., Westbrook, J., Feng, Z., Gilliland, G., Bhat, T.N., Weissig, H., Shindyalov, I.N., Bourne, P.E., 2000. The Protein Data Bank. Nucleic Acids Res 28 (1), 235–242. https://doi.org/10.1093/nar/28.1.235.

BIOVIA; Dassault Systèmes; Discovery Studio (2021); San Diego; CA, USA.

Burley, S.K., Berman, H.M., Christie, C., et al., 2018. RCSB Protein Data Bank: Sustaining a living digital data resource that enables breakthroughs in scientific research and biomedical education. Protein Sci. 27 (1), 316–330. https://doi.org/10.1002/pro.3331.

Burley, S.K., Berman, H.M., Kleywegt, G.J., Markley, J.L., Nakamura, H., Velankar, S., 2017. Protein Data Bank (PDB): The Single Global Macromolecular Structure Archive. Methods Mol. Biol. 1607, 627–641. https://doi.org/10.1007/978-1-4939-7000-1_26.

Case, D.A., Aktulga, H.M., Belfon, K., Cerutti, D.S., Cisneros, G.A., Cruzeiro, V.W., Forouzesh, N., Giese, T.J., Götz, A.W., Gohlke, H., Izadi, S., 2023. AmberTools. J. Chem. Inf. Model. 63 (20), 6183–6191. https://doi.org/10.1021/acs.jcim.3c01153.

Cavalli, A., Poluzzi, E., De Ponti, F., Recanatini, M., 2002. Toward a pharmacophore for drugs inducing the long QT syndrome: insights from a CoMFA study of HERG K^{+} channel blockers. J. Med Chem. 45 (18), 3844–3853. https://doi.org/10.1021/jm0208875.

Chemical Computing Group, 2016. version. Mol., Oper. Environ. (MOE) 08, 2016.

Chen, Y.C., 2015. Beware of docking! Trends Pharm. Sci. 36 (2), 78–95. https://doi.org/10.1016/j.tips.2014.12.001.

Chhetri, B.K., Tedbury, P.R., Sweeney-Jones, A.M., Mani, L., Soapi, K., Manfredi, C., Sorscher, E., Sarafianos, S.G., Kubanek, J., 2022. Marine Natural Products as Leads against SARS-CoV-2 Infection. J. Nat. Prod. 85 (3), 657–665. https://doi.org/10.1021/acs.jnatprod.2c00015.

Daina, A., Michielin, O., Zoete, V., 2017. SwissADME: a free web tool to evaluate pharmacokinetics, drug-likeness and medicinal chemistry friendliness of small molecules. Sci. Rep. 7, 42717 https://doi.org/10.1038/srep42717.

Davis, R.A., Beattie, K.D., Xu, M., Yang, X., Yin, S., Holla, H., Healy, P.C., Sykes, M., Shelper, T., Avery, V.M., Elofsson, M., Sundin, C., Quinn, R.J., 2014. Solving the supply of resveratrol tetramers from Papua New Guinean rainforest anisoptera species that inhibit bacterial type III secretion systems. J. Nat. Prod. 77 (12), 2633–2640. https://doi.org/10.1021/np500433z.

De Ponti, F., Poluzzi, E., Montanaro, N., 2001. Organising evidence on QT prolongation and occurrence of Torsades de Pointes with non-antiarrhythmic drugs: a call for consensus. Eur. J. Clin. Pharm. 57 (3), 185–209. https://doi.org/10.1007/s002280100290.

Divsalar, D.N., Simoben, C.V., Schonhofer, C., Richard, K., Sippl, W., Ntie-Kang, F., Tietjen, I., 2020. Novel histone deacetylase inhibitors and HIV-1 latency-reversing agents identified by large-scale virtual screening. Front Pharmacol. 2020 11, 905. https://doi.org/10.3389/fphar.2020.00905.

Ebob, O.T., Babiaka, S.B., Ntie-Kang, F., 2021. Natural products as potential lead compounds for drug discovery against SARS-CoV-2. Nat. Prod. Bioprospect. 11 (6), 611–628. https://doi.org/10.1007/s13659-021-00317-w.

Esmaielbeiki, R., Nebel, J.C., 2014. Scoring docking conformations using predicted protein interfaces. BMC Bioinformatics. 15, 171. https://doi.org/10.1186/1471-2105-15-171.

Ferreira, L.G., Dos Santos, R.N., Oliva, G., Andricopulo, A.D., 2015. Molecular docking and structure-based drug design strategies. Molecules 20 (7), 13384–13421. https://doi.org/10.3390/molecules200713384.

Forouzesh, N., Izadi, S., Onufriev, A.V., 2017. Grid-Based Surface Generalized Born Model for Calculation of Electrostatic Binding Free Energies. J. Chem. Inf. Model 57 (10), 2505–2513. https://doi.org/10.1021/acs.jcim.7b00192.

García-Iriepa, C., Hognon, C., Francés-Monerris, A., et al., 2020. Thermodynamics of the Interaction between the Spike Protein of Severe Acute Respiratory Syndrome Coronavirus-2 and the Receptor of Human Angiotensin-Converting Enzyme 2. Effects of Possible Ligands. J. Phys. Chem. Lett. 11 (21), 9272–9281. https://doi.org/10.1021/acs.jpclett.0c02203.

Ghosh, R., Chakraborty, A., Biswas, A., Chowdhuri, S., 2021. Evaluation of green tea polyphenols as novel coronavirus (SARS CoV-2) main protease (M^{pro}) inhibitors - an *in silico* docking and molecular dynamics simulation study. J. Biomol. Struct. Dyn. 39 (12), 4362–4374. https://doi.org/10.1080/07391102.2020.1779818.

Guo, Z., Cheng, Y., Huang, W., Jiao, R., 2020. Shoreanol A and B, unprecedented oligostilbenoids from the twigs of *Shorea obtusa* Wall. Fitoterapia 142, 104502. https://doi.org/10.1016/j.fitote.2020.104502.

Halgren, T.A., 1999. MMFF VII. Characterization of MMFF94, MMFF94s, and other widely available force fields for conformational energies and for intermolecular-interaction energies and geometries. J. Comput. Chem. 20 (7), 730–748. https://doi.org/10.1002/(SICI)1096-987X(199905)20:7.

Halgren, T.A., Murphy, R.B., Friesner, R.A., et al., 2004. Glide: a new approach for rapid, accurate docking and scoring. 2. Enrichment factors in database screening. J. Med Chem. 47 (7), 1750–1759. https://doi.org/10.1021/jm030644s.

Horvath, D., 2011. Pharmacophore-based virtual screening. Methods Mol. Biol. 672, 261–298. https://doi.org/10.1007/978-1-60761-839-3_11.

Humphrey, W., Dalke, A., Schulten, K., 1996. VMD: visual molecular dynamics. J. Mol. Graph 14 (1), 33–38. https://doi.org/10.1016/0263-7855(96)00018-5.

Irvine, J.D., Takahashi, L., Lockhart, K., Cheong, J., Tolan, J.W., Selick, H.E., Grove, J.R., 1999. MDCK (Madin-Darby canine kidney) cells: A tool for membrane permeability screening. J. Pharm. Sci. 88 (1), 28–33. https://doi.org/10.1021/js9803205.

Istifli, E.S., Netz, P.A., Sihoglu Tepe, A., Sarikurkcu, C., Tepe, B., 2022. Understanding the molecular interaction of SARS-CoV-2 spike mutants with ACE2 (angiotensin converting enzyme 2). J. Biomol. Struct. Dyn. 40 (23), 12760–12771. https://doi.org/10.1080/07391102.2021.1975569.

Ito, T., Tanaka, T., Ido, Y., Nakaya, K.I., Iinuma, M., Riswan, S., 2000. Stilbenoids isolated from stem bark of Shorea hemsleyana. Chem. Pharm. Bull. (Tokyo) 48 (7), 1001–1005. https://doi.org/10.1248/cpb.48.1001.

Jackson, C.B., Farzan, M., Chen, B., Choe, H., 2022. Mechanisms of SARS-CoV-2 entry into cells. Nat. Rev. Mol. Cell Biol. 23 (1), 3–20. https://doi.org/10.1038/s41580-021-00418-x.

Jakalian, A., Bush, B.L., Jack, D.B., Bayly, C.I., 2000. Fast, efficient generation of high-quality atomic charges. AM1-BCC model: I. Method. J. Comput. Chem. 21 (2), 132–146. https://doi.org/10.1002/(SICI)1096-987X(20000130)21:2%3C132::AID-JCC5%3E3.0.CO;2-P.

Kayser, O., Kiderlen, A.F., Croft, S.L., 2003. Natural products as antiparasitic drugs. Parasitol. Res 90 (Suppl 2), S55–S62. https://doi.org/10.1007/s00436-002-0768-3.

Kontoyianni, M., 2017. Docking and Virtual Screening in Drug Discovery. Methods Mol. Biol. 1647, 255–266. https://doi.org/10.1007/978-1-4939-7201-2_18.

Kumar, R., Bidgood, C.L., Levrier, C., Gunter, J.H., Nelson, C.C., Sadowski, M.C., Davis, R.A., 2020. Synthesis of a Unique Psammaplysin F Library and Functional Evaluation in Prostate Cancer Cells by Multiparametric Quantitative Single Cell Imaging. Aug 28 J. Nat. Prod. 83 (8), 2357–2366. https://doi.org/10.1021/acs.jnatprod.0c00121.

Lam, K.S., 2007. New aspects of natural products in drug discovery. Trends Microbiol 15 (6), 279–289. https://doi.org/10.1016/j.tim.2007.04.001.

Lan, J., Ge, J., Yu, J., Shan, S., Zhou, H., Fan, S., Zhang, Q., Shi, X., Wang, Q., Zhang, L., Wang, X., 2020. Structure of the SARS-CoV-2 spike receptor-binding domain bound to the ACE2 receptor. Nature 581 (7807), 215–220. https://doi.org/10.1038/s41586-020-2180-5.

Li, X., Yuan, H., Li, X., Wang, H., 2023. Spike protein mediated membrane fusion during SARS-CoV-2 infection. J. Med Virol. 95 (1), e28212 https://doi.org/10.1002/jmv.28212.

Lin, W.-H., Fang, J.-M., Cheng, Y.-S., 1999. Lignans from *Taiwania cryptomerioides*. Phytochemistry 50 (4), 653–658. https://doi.org/10.1016/S0031-9422(98)00577-9.

Lionta, E., Spyrou, G., Vassilatis, D.K., Cournia, Z., 2014. Structure-based virtual screening for drug discovery: principles, applications and recent advances. Curr. Top. Med Chem. 14 (16), 1923–1938. https://doi.org/10.2174/1568026614666140929124445.

Lohning, A.E., Levonis, S.M., Williams-Noonan, B., Schweiker, S.S., 2017. A Practical Guide to Molecular Docking and Homology Modelling for Medicinal Chemists. Curr. Top. Med Chem. 17 (18), 2023–2040. https://doi.org/10.2174/1568026617666170130110827.

Lupala, C.S., Ye, Y., Chen, H., Su, X.D., Liu, H., 2022. Mutations on RBD of SARS-CoV-2 Omicron variant result in stronger binding to human ACE2 receptor. Biochem Biophys. Res Commun. 590, 34–41. https://doi.org/10.1016/j.bbrc.2021.12.079.

Macalino, S.J., Gosu, V., Hong, S., Choi, S., 2015. Role of computer-aided drug design in modern drug discovery. Arch. Pharm. Res 38 (9), 1686–1701. https://doi.org/10.1007/s12272-015-0640-5.

Maier, J.A., Martinez, C., Kasavajhala, K., Wickstrom, L., Hauser, K.E., Simmerling, C., 2015. ff14SB: improving the accuracy of protein side chain and backbone parameters from ff99SB. J. Chem. Theory Comput. 11 (8), 3696–3713. https://doi.org/10.1021/acs.jctc.5b00255.

Majoumo-Mbe, F., Sangbong, N.A., Tcho, A.T., Namba-Nzanguim, C.T., Simoben, C.V., Eni, D.B., Isa, M.A., Poli, A.N.R., Cassel, J., Salvino, J.M., Montaner, L.J., Tietjen, I., Ntie-Kang, F., 2024. 5-chloro-3-(2-(2,4-dinitrophenyl) hydrazono)indolin-2-one: synthesis, characterization, biochemical and computational screening against SARS-CoV-2. Chem. Pap. https://doi.org/10.1007/s11696-023-03274-5.

Meek, A., Weaver, D.F., 2022. Drug-receptor interactions: it is a numbers game. Can. J. Neurol. Sci. 49 (4), 589–590. https://doi.org/10.1017/cjn.2021.152.

Morris, G.M., Lim-Wilby, M., 2008. Molecular docking. Methods Mol. Biol. 443, 365–382. https://doi.org/10.1007/978-1-59745-177-2_19.

Moumbock, A.F.A., Tran, H.T.T., Lamy, E., Günther, S., 2023. BC-11 is a covalent TMPRSS2 fragment inhibitor that impedes SARS-CoV-2 host cell entry. Arch. Pharm. (Weinh. 356 (1), e2200371 https://doi.org/10.1002/ardp.202200371.

Nassiri-Asl, M., Hosseinzadeh, H., 2016. Review of the pharmacological effects of *Vitis vinifera* (Grape) and its bioactive constituents: an update. Phytother. Res 30 (9), 1392–1403. https://doi.org/10.1002/ptr.5644.

NCATS (2020) Spike-ACE2 protein-protein interaction (AlphaLISA). In: SARS-CoV-2 Assays [Internet]. Bethesda (MD): National Center for Advancing Translational Sciences. PMID: 35512044.

Newman, D.J., Cragg, G.M., 2009. Natural product scaffolds as leads to drugs. Future Med Chem. 1 (8), 1415–1427. https://doi.org/10.4155/fmc.09.113.

Newman, D.J., Cragg, G.M., 2020. Natural products as sources of new drugs over the nearly four decades from 01/1981 to 09/2019. J. Nat. Prod. 83 (3), 770–803. https://doi.org/10.1021/acs.jnatprod.9b01285.

Ntie-Kang, F., Simoben, C.V., Karaman, B., Ngwa, V.F., Judson, P.N., Sippl, W., Mbaze, L. M., 2016. Pharmacophore modeling and in silico toxicity assessment of potential anticancer agents from African medicinal plants. Drug Des. Develop. Ther. 10, 2137–2154. https://doi.org/10.2147/DDDT.S108118.

Ntie-Kang, F., Kannan, S., Wichapong, K., Owono Owono, L.C., Sippl, W., Megnassan, E., 2014. Binding of pyrazole-based inhibitors to *Mycobacterium tuberculosis* pantothenate synthetase: docking and MM-GB(PB)SA analysis. Mol. Biosyst. 10 (2), 223–239. https://doi.org/10.1039/c3mb70449a.

Ntie-Kang, F., Telukunta, K.K., Döring, K., Simoben, C.V., Moumbock, A., Malange, A.F., Njume, Y.I., Yong, L.E., Sippl, J.N., Günther, W., NANPDB, S., 2017. A resource for natural products from Northern African Sources. J. Nat. Prod. 80 (7), 2067–2076. https://doi.org/10.1021/acs.jnatprod.7b00283.

Omrani, M., Keshavarz, M., Nejad Ebrahimi, S., Mehrabi, M., McGaw, L.J., Ali Abdalla, M., Mehrbod, P., 2021. Potential natural products against respiratory viruses: a perspective to develop anti-COVID-19 medicines. Front Pharm. 11, 586993 https://doi.org/10.3389/fphar.2020.586993.

Onguéné, P.A., Simoben, C.V., Fotso, G.W., Andrae-Marobela, K., Khalid, S.A., Ngadjui, B.T., Mbaze, L.M., Ntie-Kang, F., 2018. In silico toxicity profiling of natural product compound libraries from African flora with anti-malarial and anti-HIV properties. Comput. Biol. Chem. 72, 136–149. https://doi.org/10.1016/j.compbiolchem.2017.12.002.

Pipitò, L., Rujan, R.M., Reynolds, C.A., Deganutti, G., 2022. Molecular dynamics studies reveal structural and functional features of the SARS-CoV-2 spike protein. Bioessays 44 (9), e2200060. https://doi.org/10.1002/bies.202200060.

Pires, D.E., Blundell, T.L., Ascher, D.B., 2015. pkCSM: predicting small-molecule pharmacokinetic and toxicity properties using graph-based signatures. J. Med Chem. 58 (9), 4066–4072. https://doi.org/10.1021/acs.jmedchem.5b00104.

Raimundo E Silva, J.P., Acevedo, C.A.H., de Souza, T.A., de Menezes, R.P.B., Sessions, Z. L., Abreu, L.S., Cibulski, S.P., Scotti, L., da Silva, M.S., Muratov, E.N., Scotti, M.T., Tavares, J.F., 2021. Natural Products as Potential Agents against SARS-CoV- 2. Curr. Med Chem. 28 (27), 5498–5526. https://doi.org/10.2174/0929867328666210125113938.

Rivière, C., Pawlus, A.D., Mérillon, J.M., 2012. Natural stilbenoids: distribution in the plant kingdom and chemotaxonomic interest in Vitaceae. Nat. Prod. Rep. 29 (11), 1317–1333. https://doi.org/10.1039/c2np20049j.

Roche V.F., Zito S.W., Lemke T.L., Williams D.A. (Eds). Foye's Principles of Medicinal Chemistry; 8th ed.; Wolters Kluwer Health; 8th edition. 2019, Philadelphia, PA.

Roe, D.R., Cheatham III, T.E., 2013. PTRAJ and CPPTRAJ: software for processing and analysis of molecular dynamics trajectory data. J. Chem. Theory Comput. 9 (7), 3084–3095. https://doi.org/10.1021/ct400341p.

Rogers, D.M., Agarwal, R., Vermaas, J.V., Smith, M.D., Rajeshwar, R.T., Cooper, C., Sedova, A., Boehm, S., Baker, M., Glaser, J., Smith, J.C., 2023. SARS-CoV2 billion-compound docking. Sci. Data 10 (1), 173. https://doi.org/10.1038/s41597-023-01984-9.

Saied, E.M., El-Maradny, Y.A., Osman, A.A., Darwish, A.M.G., Abo Nahas, H.H., Niedbała, G., Piekutowska, M., Abdel-Rahman, M.A., Balbool, B.A., Abdel-Azeem, A. M., 2021. A comprehensive review about the molecular structure of severe acute respiratory syndrome coronavirus 2 (SARS-CoV-2): insights into natural products against COVID-19. Pharmaceutics 13 (11), 1759. https://doi.org/10.3390/pharmaceutics13111759.

Sciabola, S., Torella, R., Nagata, A., Boehm, M., 2022. Critical Assessment of State-of-the-Art Ligand-Based Virtual Screening Methods. Mol. Inf. 41 (11), e2200103 https://doi.org/10.1002/minf.202200103.

Shelley, J.C., Cholleti, A., Frye, L.L., Greenwood, J.R., Timlin, M.R., Uchimaya, M., 2007. Epik: a software program for pK a prediction and protonation state generation for drug-like molecules. J. Comput.-Aided Mol. Des. 21, 681–691. https://doi.org/10.1007/s10822-007-9133-z.

Shu, Y.Z., 1998. Recent natural products based drug development: a pharmaceutical industry perspective. J. Nat. Prod. 61 (8), 1053–1071. https://doi.org/10.1021/np9800102.

Simoben, C.V., Qaseem, A., Moumbock, A.F.A., Telukunta, K.K., Günther, S., Sippl, W., Ntie-Kang, F., 2020. Pharmacoinformatic investigation of medicinal plants from East Africa. Mol. Inf. 39 (11), e2000163 https://doi.org/10.1002/minf.202000163.

Simoben, C.V., Ghazy, E., Zeyen, P., Darwish, S., Schmidt, M., Romier, C., Robaa, D., Sippl, W., 2021. Binding free energy (BFE) calculations and quantitative structure–activity relationship (QSAR) analysis of *Schistosoma mansoni* histone deacetylase 8 (smHDAC8) inhibitors. Molecules 26 (9), 2584. https://doi.org/10.3390/molecules26092584.

Simoben, C.V., Robaa, D., Chakrabarti, A., Schmidtkunz, K., Marek, M., Lancelot, J., Kannan, S., Melesina, J., Shaik, T.B., Pierce, R.J., Romier, C., 2018. A novel class of *Schistosoma mansoni* histone deacetylase 8 (HDAC8) inhibitors identified by structure-based virtual screening and in vitro testing. Molecules 23 (3), 566. https://doi.org/10.3390/molecules23030566.

Schrödinger, Maestro, Release version 2017-2.

Shadrack, D.M., Deogratias, G., Kiruri, L.W., Onoka, I., Vianney, J.M., Swai, H., Nyandoro, S.S., 2021. Luteolin: a blocker of SARS-CoV-2 cell entry based on relaxed complex scheme, molecular dynamics simulation, and metadynamics. J. Mol. Model 27 (8), 221. https://doi.org/10.1007/s00894-021-04833-x.

Stenberg, P., Norinder, U., Luthman, K., Artursson, P., 2001. Experimental and computational screening models for the prediction of intestinal drug absorption. J. Med Chem. 44 (12), 1927–1937. https://doi.org/10.1021/jm001101a.

Tanaka, T., Ito, T., Ido, Y., Son, T.K., Nakaya, K., Iinuma, M., Ohyama, M., Chelladurai, V., 2000. Stilbenoids in the stem bark of Hopea parviflora. Phytochemistry 53 (8), 1015–1019. https://doi.org/10.1016/s0031-9422(00)00019-4.

Tanimoto, S., Itoh, S.G., Okumura, H., 2022. State-of-the-art molecular dynamics simulation studies of RNA-dependent RNA polymerase of SARS-CoV-2. Int. J. Mol. Sci. 23 (18), 10358. https://doi.org/10.3390/ijms231810358.

Tang, S., Kim, P.S., 2019. A high-affinity human PD-1/PD-L2 complex informs avenues for small-molecule immune checkpoint drug discovery. Proc. Natl. Acad. Sci. (USA) 116 (49), 24500–24506. https://doi.org/10.1073/pnas.1916916116.

Tietjen, I., Cassel, J., Register, E.T., Zhou, X.Y., Messick, T.E., Keeney, F., Lu, L.D., Beattie, K.D., Rali, T., Tebas, P., Ertl, H.C.J., Salvino, J.M., Davis, R.A., Montaner, L. J., 2021. The natural stilbenoid (-)-hopeaphenol inhibits cellular entry of SARS-CoV-2 USA-WA1/2020, B.1.1.7, and B.1.351 variants. Antimicrob. Agents Chemother. 65 (12), e0077221 https://doi.org/10.1128/AAC.00772-21.

Tripathi, N.M., Bandyopadhyay, A., 2022. High throughput virtual screening (HTVS) of peptide library: technological advancement in ligand discovery. Eur. J. Med. Chem. 243, 114766 https://doi.org/10.1016/j.ejmech.2022.114766.

Urbina, F., Lowden, C.T., Culberson, J.C., Ekins, S., 2022. MegaSyn: integrating generative molecular design, automated analog designer, and synthetic viability prediction. ACS Omega 7 (22), 18699–18713. https://doi.org/10.1021/acsomega.2c01404.

Ursu, O., Rayan, A., Goldblum, A., Oprea, T.I., 2011. Understanding drug-likeness. Wiley Interdiscip. Rev.: Comput. Mol. Sci. 1, 760–781. https://doi.org/10.1002/wcms.52.

Vázquez, J., López, M., Gibert, E., Herrero, E., Luque, F.J., 2020. Merging Ligand-based and structure-based methods in drug discovery: an overview of combined virtual screening approaches. Molecules 25 (20), 4723. https://doi.org/10.3390/molecules25204723.

Vistoli, G., Pedretti, A., Testa, B., 2008. Assessing drug-likeness–what are we missing? Drug Discov. Today 13 (7-8), 285–294. https://doi.org/10.1016/j.drudis.2007.11.007.

Vuai, S.A.H., Ogedjo, M.M., Isaac, O., Sahini, M.G., Swai, H.S., Shadrack, D.M., 2022. Relaxed complex scheme and molecular dynamics simulation suggests small molecule inhibitor of human TMPRSS2 for combating COVID-19. J. Biomol. Struct. Dyn. 40 (24), 13925–13935. https://doi.org/10.1080/07391102.2021.1997817.

Watts, K.S., Dalal, P., Murphy, R.B., Sherman, W., Friesner, R.A., Shelley, J.C., 2010. ConfGen: a conformational search method for efficient generation of bioactive conformers. J. Chem. Info Model 50 (4), 534–546. https://doi.org/10.1021/ci100015j.

Wermuth, C.G., 2006. Similarity in drugs: reflections on analogue design. Drug Discov. Today 11 (7-8), 348–354. https://doi.org/10.1016/j.drudis.2006.02.006.

Williams-Noonan, B.J., Todorova, N., Kulkarni, K., Aguilar, M.I., Yarovsky, I., 2021. An active site inhibitor induces conformational penalties for ACE2 recognition by the spike protein of SARS-CoV-2. J. Phys. Chem. B 125 (10), 2533–2550. https://doi.org/10.1021/acs.jpcb.0c11321.

Wrobel, A.G., 2023. Mechanism and evolution of human ACE2 binding by SARS-CoV-2 spike. Curr. Opin. Struct. Biol. 81, 102619 https://doi.org/10.1016/j.sbi.2023.102619.

Wu, S.Y., Fu, Y.H., Zhou, Q., Bai, M., Chen, G.Y., Han, C.R., Song, X.P., 2019. Biologically active oligostilbenes from the stems of *Vatica mangachapoi* and chemotaxonomic significance. Nat. Prod. Res 33 (16), 2300–2307. https://doi.org/10.1080/14786419.2018.1443091.

Yazdanian, M., Glynn, S.L., Wright, J.L., Hawi, A., 1998. Correlating partitioning and caco-2 cell permeability of structurally diverse small molecular weight compounds (Sep). Pharm. Res 15 (9), 1490–1494. https://doi.org/10.1023/a:1011930411574.

Yesudhas, D., Srivastava, A., Gromiha, M.M., 2021. COVID-19 outbreak: history, mechanism, transmission, structural studies and therapeutics. Infection 49 (2), 199–213. https://doi.org/10.1007/s15010-020-01516-2.

Zak, K.M., Kitel, R., Przetocka, S., Golik, P., Guzik, K., Musielak, B., Dömling, A., Dubin, G., Holak, T.A., 2015. Structure of the Complex of Human Programmed Death 1, PD-1, and Its Ligand PD-L1. Structure 23 (12), 2341–2348. https://doi.org/10.1016/j.str.2015.09.010.

Zulfiqar, B., Jones, A.J., Sykes, M.L., Shelper, T.B., Davis, R.A., Avery, V.M., 2017. Screening a Natural Product-Based Library against Kinetoplastid Parasites. Molecules 22 (10), 1715. https://doi.org/10.3390/molecules22101715.